Available online at www.sciencedirect.com

ScienceDirect

Geochimica et Cosmochimica Acta 186 (2016) 242–276

Geochimica et Cosmochimica Acta

www.elsevier.com/locate/gca

Oxygen isotopic variations in the outer margins and Wark–Lovering rims of refractory inclusions

Justin I. Simon [a,*], Jennifer E.P. Matzel [b], Steven B. Simon [c], Ian D. Hutcheon [b,1], D. Kent Ross [a,d], Peter K. Weber [b], Lawrence Grossman [c,e]

[a] *Center for Isotope Cosmochemistry and Geochronology, Astromaterials Research and Exploration Science Division, Exploration, Integration, and Science Directorate, NASA Johnson Space Center, Houston, TX 77058, United States*
[b] *Lawrence Livermore National Laboratory, Livermore, CA 94451, United States*
[c] *Department of the Geophysical Sciences, The University of Chicago, 5734 S. Ellis Ave, Chicago, IL 60637, United States*
[d] *University of Texas at El Paso/Jacobs Technology, Houston, TX 77058, United States*
[e] *Enrico Fermi Institute, The University of Chicago, Chicago, IL 60637, United States*

Received 13 July 2015; accepted in revised form 14 April 2016; available online 2 May 2016

Abstract

Oxygen isotopic variations across the outer margins and Wark–Lovering (WL) rims of a diverse suite of six coarse-grained Types A and B refractory inclusions from both oxidized and reduced CV3 chondrites suggest that CAIs originated from a ^{16}O-rich protosolar gas reservoir and were later exposed to both relatively ^{17,18}O-rich and ^{16}O-rich reservoirs. The O-isotope profiles of CAIs can be explained by changes in the composition of gas near the protoSun or the migration of CAIs through a heterogeneous nebula. Variability within the inclusion interiors appears to have been set prior to WL rim growth. Modeling the isotopic zoning profiles as diffusion gradients between inclusion interiors and edges establishes a range of permissible time–temperature combinations for their exposure in the nebula. At mean temperatures of 1400 K, models that match the isotope gradients in the inclusions yield timescales ranging from 5×10^3 to 3×10^5 years. Assuming CAIs originated with a relatively ^{16}O-rich (protosolar) isotopic composition, differences among the melilite interiors and the isotopic gradients in their margins imply the existence of a number of isotopically distinct reservoirs. Evidence at the edges of some CAIs for subsequent isotopic exchange may relate to the beginning of rim formation. In the WL rim layers surrounding the interiors, spinel is relatively ^{16}O-rich but subtly distinct among different CAIs. Melilite is often relatively ^{16}O-poor, but rare relatively ^{16}O-rich grains also exist. Pyroxene generally exhibits intermediate O-isotope compositions and isotopic zoning. Olivine in both WL and accretionary rims, when present, is isotopically heterogeneous. The extreme isotopic heterogeneity among and within individual WL rim layers and in particular, the observed trends of outward ^{16}O-enrichments, suggest that rims surrounding CAIs contained in CV3 chondrites, like the inclusions themselves, formed from a number of isotopically distinct gas reservoirs. Collectively, these results support numerical protoplanetary disk models in which CAIs were transported between several distinct nebular reservoirs multiple times prior to accretion onto a parent body.

Keywords: Oxygen isotopes; CAIs; Wark-Lovering rims; NanoSIMS; Protoplanetary disk

1. INTRODUCTION

Calcium–aluminum-rich inclusions (CAIs) have refractory mineral assemblages consisting of phases predicted to condense from a hot nebula of solar composition

* Corresponding author.
E-mail address: justin.i.simon@nasa.gov (J.I. Simon).
[1] Deceased.

http://dx.doi.org/10.1016/j.gca.2016.04.025
0016-7037/Published by Elsevier Ltd.

(e.g., Grossman, 1972). We now understand that the mineralogy of coarse-grained CAIs is the result of crystallization from melts and that their reset Al–Mg chronologies (MacPherson et al., 2012) and decoupled stable isotope compositions of refractory and more volatile elements (Simon and DePaolo, 2010) likely reflect substantial processing of primordial condensates. Despite evidence for a complicated history, their old ages (Amelin et al., 2002; Bouvier and Wadhwa, 2010; Connelly et al., 2012) attest to the fact that they represent some of the most primitive solar system materials and likely provide our best window into the earliest conditions of the solar protoplanetary disk. After crystallization of their interiors, most inclusions were rimmed by a common mineral layering sequence, implying a fundamental change in their environment. Previous investigations have interpreted these Wark–Lovering (WL) rims (Wark and Lovering, 1977) as products of formation from nebular reservoirs with pressures (Simon et al., 2005), temperatures (Young et al., 2005), and isotopic compositions (Krot et al., 2002; Aleon et al., 2007; Yurimoto et al., 1998; Yoshitake et al., 2005; Simon et al., 2011) distinct from those indicated by the interiors. These environmental changes likely not only produced the mineralogical variability of WL rims (Dyl et al., 2011; Simon et al., 2005), but could also have led to mineralogical (Keller and Buseck, 1991; Metzler et al., 1992) and isotopic (Fagan et al., 2004a; Simon and Young, 2011) changes within the refractory inclusions themselves.

Compared to the terrestrial planets, many CAIs exhibit an ^{16}O-rich composition ($\delta^{18}O \approx \delta^{17}O \leqslant -40‰$) that likely reflects the O-isotopic composition of protosolar gas in the nebula (McKeegan et al., 2011). Yet, it has been known for decades that individual CAIs have heterogeneous O-isotopic compositions, in some cases spanning the range between protosolar to planetary reservoirs (Clayton et al., 1977). One can postulate that CAIs condensed, melted, crystallized, and were rimmed in the relatively ^{16}O-rich protosolar reservoir, and that any internal O-isotopic heterogeneity resulted from mineralogically controlled isotope exchange with a planetary reservoir ($\delta^{18}O \sim 0‰$) on the chondrite parent body, e.g., Wasson et al. (2001). Alternatively, the O-isotopic heterogeneity in CAIs can be explained by formation from both relatively ^{16}O-rich and ^{16}O-poor reservoirs of nebular gas (Clayton et al., 1977; Yurimoto et al., 1998; Krot et al., 2002; Yoshitake et al., 2005; Aleon et al., 2007; Simon et al., 2011). This might occur if igneous CAIs formed through admixing melanges of isotopically heterogeneous material and/or through transport, exposure, and exchange with distinct nebular reservoirs. As of yet the locations and identities of the reservoirs, the formation processes involved in recording the isotopic shifts, and the timing of isotopic exchange are not well-constrained.

In a prior study (Simon et al., 2011), secondary ion mass spectrometry (SIMS) measurements of the outer margin and WL rim of the Allende compact Type A CAI A37 revealed large O-isotope heterogeneity across the outermost ~70 μm of the inclusion and showed >25‰ variations in $\Delta^{17}O$ (departure from the terrestrial mass fractionation line; $\Delta^{17}O = \delta^{17}O - 0.52 \times \delta^{18}O$) within the ~100 μm-thick WL rim. Those workers proposed that the variations reflected either transport of the inclusion between distinct nebular reservoirs inherited from the parental molecular cloud, or a time-varying oxygen isotopic composition of a region of the nebula, such as the relatively ^{16}O-poor gas predicted for the outer margins of the disk by photochemical self-shielding models (Lyons and Young, 2005). Although some rims surrounding CAIs exhibit extreme O-isotopic heterogeneity, others are isotopically homogeneous (Matzel et al., 2013; Bodénan et al., 2014). It is noteworthy that some rims consist of only a single pyroxene layer (e.g., Bodénan et al., 2014), while others are far more complex, such as the WL rim surrounding Leoville CAI L6 (this study) that consists of at least 9 distinct mineral layers. In order to address this discrepancy, studies such as ours that involve inclusions with more complex rims and textural evidence spanning a range of formation processes are needed to evaluate solar protoplanetary disk evolution models, such as those of Cuzzi et al. (2003), Boss (2004), and Ciesla (2007).

The nature of chondritic host rocks and the potentially disparate formation histories of their constituent components create challenges to interpretation of the O-isotopic records of individual CAIs. In particular, parent body alteration may produce O-isotope heterogeneity. To document O-isotopic heterogeneity to test models for the evolution of the protoplanetary disk, this work presents the results of coordinated high-spatial resolution oxygen and petrologic investigations of CAIs with a range of mineralogical compositions and alteration histories from the Allende, Efremovka, and Leoville CV3 chondrites.

2. METHODS

2.1. Oxygen isotopic zoning profiles by NanoSIMS

Oxygen isotope measurements were performed using the NanoSIMS 50 at Lawrence Livermore National Laboratory (LLNL), following the method developed by Simon et al. (2011), during ~5 weeks of analysis over an ~3-year period (Table 1, Appendix I). Measurements were performed by sputtering the polished surfaces of CAIs in carbon-coated thin sections and epoxy embedded thick sections with a 16 keV, ~12 pA Cs^+ beam focused to a ~100 nm spot size and rastered over 2 × 2 μm regions. Negative secondary ions of $^{16}O^-$, $^{17}O^-$, $^{18}O^-$, and $^{28}Si^-$ (or $^{30}Si^-$) were collected in a Faraday cup and three separate electron multipliers, respectively. Each measurement comprises (3–6) × 10^5 counts of $^{17}O^-$ and (1.5–3.0) × 10^6 counts of $^{18}O^-$ collected during a 368-s analysis time. The data were corrected for detector dead time. Measured uncertainties reflect the standard deviation of isotope ratio data acquired over 300 rastered measurement cycles and follow a Poisson distribution. Uncertainties reported in Table 1 reflect a combination of counting statistics and either 2 standard errors (se), or 2 standard deviations (sd) of the average value of the measured mineral standards used for sample-standard bracketing (Appendices I and II). A mass resolving power of ~7000 was used to resolve $^{17}O^-$ from $^{16}OH^-$. Monitoring the $Si^-/^{16}O^-$ ratio (in addition to pre- and post-analysis

Table 1

NSpot	Mineral	From edge of inclusion (μm)	$\delta^{18}O/^{16}O$*	2σ (‰)*	$\delta^{17}O/^{16}O$*	2σ (‰)*	$\Delta^{17}O$*	2σ (‰)*	$\Delta^{17}O$**	2σ (‰)**	$^{28}Si/^{16}O$
A37_sp_2	Spinel	660	−37.2	2.4	−48.6	4.3	−29.2	4.5	−29.4	5.8	5.5E−06
A37_sp_3	Spinel	660	−34.2	2.4	−46.1	4.4	−28.4	4.5	−28.5	5.8	8.7E−07
A37_mel_1	Melilite	661	−11.3	1.9	−21.9	3.9	−16.0	4.1	−17.5	5.2	9.9E−04
A37_mel_2	Melilite	661	−12.7	2.0	−21.6	3.9	−14.9	4.1	−16.5	5.2	9.4E−04
A37_sp_1	Spinel	825	−39.3	2.5	−51.5	5.5	−31.1	5.7	−31.2	6.8	5.5E−06
Egg-6 oxygen isotope data											
Spot	Mineral	From edge of inclusion (μm)	$\delta^{18}O/^{16}O$*	2σ (‰)*	$\delta^{17}O/^{16}O$*	2σ (‰)*	$\Delta^{17}O$*	2σ (‰)*	$\Delta^{17}O$**	2σ (‰)**	$^{28}Si/^{16}O$
Traverse 1 (August 2011)											
Egg6_1	Spinel (Fe)	−38	−40.7	2.2	−45.0	3.8	−23.8	3.9	−23.9	5.5	
Egg6_2	Perovskite	−24	−14.2	1.9	−17.8	3.0	−10.4	3.2	−10.5	5.0	
Egg6_3	Spinel	−11	−35.8	2.4	−37.8	3.5	−19.2	3.7	−19.3	5.4	
Egg6_4	Plagioclase	2	0.9	1.9	−0.8	3.8	−1.3	3.9	−2.8	5.6	
Egg6_5	Plagioclase	15	6.5	1.9	5.8	3.8	2.4	4.0	0.9	5.6	
Egg6_6	Plagioclase	28	8.3	1.9	4.5	3.9	0.2	4.0	−1.4	5.6	
Egg6_7	Melilite	41	3.6	1.9	0.3	3.8	−1.6	3.9	−3.1	5.6	
Egg6_8	Melilite	54	3.3	1.9	1.0	4.2	−0.7	4.3	−2.2	5.9	
Egg6_9	Melilite	67	4.0	1.7	2.1	3.8	0.0	3.9	−1.5	5.6	
Egg6_10	Melilite	80	5.1	1.8	1.3	3.6	−1.4	3.8	−2.9	5.5	
Egg6_0	Melilite	113	3.4	2.0	2.6	4.2	0.8	4.3	−0.7	5.9	
Egg6_1_1	Melilite	145	6.8	1.8	1.4	4.0	−2.2	4.2	−3.7	5.7	
Egg6_1b	Melilite	165	1.1	2.0	−2.6	4.1	−3.2	4.2	−4.7	5.8	
Egg6_1_2	Spinel	179	−34.8	2.2	−40.4	3.9	−22.3	4.1	−22.4	5.6	
Egg6_2b	Melilite	192	4.3	1.6	3.0	3.9	0.7	4.0	−0.8	5.6	
Egg6_1_3	Melilite	212	8.7	1.9	2.3	3.8	−2.2	4.0	−3.8	5.6	
Egg6_1_4	Melilite	244	3.9	1.8	2.9	3.7	0.9	3.8	−0.6	5.5	
Egg6_1_5	Melilite	277	2.7	1.9	0.2	3.9	−1.2	4.1	−2.7	5.7	
Egg6_1_6	Melilite	310	−1.8	2.1	−4.0	4.5	−3.1	4.7	−4.6	6.1	
Egg6_1_7	Melilite	342	7.2	1.9	5.5	3.8	1.7	4.0	0.2	5.6	
Egg6_7b	Vein grossular	355	8.5	2.0	3.1	3.7	−1.3	3.8	−2.8	5.5	
Egg6_8b	Vein grossular	395	6.3	1.9	1.3	3.7	−1.9	3.8	−3.5	5.5	
Egg6_1_9	Melilite	410	6.9	2.0	2.0	3.8	−1.6	4.0	−3.1	5.6	
Egg6_1_10	Melilite	442	7.4	1.9	4.3	3.6	0.5	3.7	−1.0	5.4	
Egg6_1_11	Melilite	475	4.9	2.0	3.4	4.1	0.8	4.2	−0.7	5.8	
Egg6_1_12	Melilite	508	6.5	1.9	3.1	4.0	−0.3	4.2	−1.9	5.8	
Traverse 2 (August 2011)											
Egg6_t2_1_1	Spinel	−25	−42.4	2.5	−43.9	4.4	−21.8	4.6	−21.9	6.0	
Egg6_t2_1_2	Spinel	−10	−41.2	2.4	−50.9	4.6	−29.4	4.8	−29.5	6.2	
Egg6_t2_1_4	Melilite	19	0.5	2.1	−0.2	3.9	−0.5	4.0	−2.0	5.6	
Egg6_t2_1_5	Melilite	34	1.6	2.0	−3.0	4.5	−3.9	4.6	−5.4	6.1	
Egg6_t2_1_6	Melilite	48	0.3	2.2	−0.9	4.5	−1.0	4.7	−2.5	6.1	
Egg6_t2_1_7	Melilite	63	−0.9	2.1	−2.5	4.2	−2.1	4.4	−3.6	5.9	
Egg6_t2_1_8	Vein grossular	78	4.1	2.2	−6.0	4.6	−8.1	4.7	−9.6	6.2	

(*continued on next page*)

Table 1 (*continued*)

NSpot	Mineral	From edge of inclusion (μm)	$\delta^{18}O/^{16}O$*	2σ (‰)*	$\delta^{17}O/^{16}O$*	2σ (‰)*	$\Delta^{17}O$*	2σ (‰)*	$\Delta^{17}O$**	2σ (‰)**	$^{28}Si/^{16}O$
Egg6_t2_1_9	Vein grossular	93	2.1	2.1	−6.7	4.1	−7.8	4.2	−9.3	5.8	
Egg6_t2_1_10	Melilite	107	−0.7	2.0	−2.3	4.2	−1.9	4.3	−3.4	5.9	
Egg6_t2b_1_1	Melilite	146	−13.2	2.2	−7.8	4.1	−1.0	4.3	−2.5	5.8	
Egg6_t2b_1_2	Melilite	184	0.5	2.0	−4.9	4.2	−5.2	4.4	−6.7	5.9	
Egg6_t2b_1_3	Vein grossular	222	6.5	2.2	2.1	4.5	−1.3	4.6	−2.9	6.1	
Egg6_t2b_1_4	Vein grossular	260	4.1	2.0	−1.3	4.1	−3.4	4.3	−4.9	5.8	
Egg6_t2b_1_5	Melilite	298	3.8	2.0	−1.6	4.0	−3.6	4.1	−5.1	5.7	
Egg6_t2b_1_6	Fassaite	337	−34.0	1.8	−36.7	3.7	−18.9	3.8	−18.1	5.5	
Egg6_t2b_1_7	Melilite	375	5.4	2.0	−3.5	4.3	−6.3	4.4	−7.8	5.9	
Egg6_t2b_1_8	Melilite	413	5.9	1.9	−1.3	4.1	−4.4	4.2	−5.9	5.8	
Egg6_t2b_1_10	Melilite	489	4.2	1.9	−2.1	4.2	−4.2	4.3	−5.8	5.9	
Egg6_t2b_1_11	Melilite	528	5.2	2.0	−2.0	4.3	−4.7	4.4	−6.2	5.9	
Egg6_t2b_1_12	Melilite	566	−0.2	1.8	−7.8	3.8	−7.7	3.9	−9.2	5.6	
Egg6_t2b_1_13	Melilite	604	4.0	2.0	−3.1	3.8	−5.2	3.9	−6.7	5.6	
Egg6_t2b_1_14	Melilite	642	3.3	2.0	−3.4	4.0	−5.2	4.1	−6.7	5.7	
Egg6_t2b_1_15	Melilite	681	4.4	1.8	−4.8	4.2	−7.0	4.3	−8.6	5.8	
Main WL-rim Traverse (December 2012)											
Egg6_spn_1	Spinel (Fe)	−41	−51.1	1.3	−49.6	3.0	−23.0	3.1	−23.7	5.1	1.08E−05
Egg6_spn_2	Spinel (Fe)	−33	−44.4	1.6	−42.2	3.3	−19.1	3.4	−19.8	5.3	8.69E−04
Egg6_spn_3	Ti-pyroxene + <spinel	−26	−11.6	2.1	−14.5	3.9	−8.5	4.0	−9.2	5.5	1.67E−02
Egg6_perov_3	Spinel > perovskite	−18	−20.7	1.2	−23.5	2.3	−12.7	2.4	−13.4	4.7	2.22E−04
Egg6_spn_4	Ti-pyroxene	−17	−8.3	1.9	−8.4	3.6	−4.1	5.3	−4.9	−4.9	2.05E−02
Egg6_spn_5	Ti-pyroxene	−11	−8.0	1.9	−6.2	3.5	−2.0	5.3	−2.8	−2.8	2.29E−02
Egg6_perov_1	Spinel + perovskite	−9	−1.1	0.9	−4.2	2.1	−3.7	2.1	−4.4	4.6	5.78E−05
Egg6_spn_6	Spinel	0	−39.5	1.8	−40.5	3.7	−19.9	3.8	−20.6	5.5	2.84E−04
Near main WL-rim Traverse (December 2012)											
Egg6_perov_5	Perovskite	−23	1.8	1.0	−1.7	2.1	−2.6	2.2	−3.3	4.6	4.19E−05
Egg6_perov_4	Perovskite	−17	−0.2	1.0	−1.3	2.0	−1.2	2.0	−1.9	4.5	4.68E−05
Egg6_perov_2	Perovskite > spinel?	−9	3.5	1.2	−2.3	2.3	−4.2	2.4	−4.9	4.7	1.78E−02
Rim Traverse Follow up (March 2013)											
Egg6_rim_1	Al-pyroxene	−47	1.6	1.6	−3.2	3.5	−4.0	3.6	−4.3	5.3	3.30E−02
Rim Traverse-1 (March 2013)											
Egg6_spn_t1_1	Spinel	−21	−49.3	1.7	−52.3	3.4	−26.6	3.4	−26.9	4.9	1.96E−05
Egg6_spn_t1_3	Spinel	−21	−43.4	1.7	−48.0	3.4	−25.3	3.4	−25.6	5.0	1.96E−05
Rim Traverse−2 (February–March 2013)											
Egg6_spn_t2_4	Al-pyroxene	−52	−17.2	1.8	−22.4	3.9	−13.4	4.0	−13.7	5.6	3.85E−02
Egg6_spn_t2_1	Spinel	−22	−45.4	1.6	−50.6	3.2	−26.9	3.2	−27.2	4.8	1.37E−04
Egg6_spn_t2_2	Spinel + melilite	−13	11.7	1.9	−0.6	4.0	−6.7	4.0	−7.0	5.4	2.41E−02
Egg6_spn_t2_3	Melilite	−2	2.9	1.7	−3.8	3.8	−5.2	3.8	−4.3	5.3	2.09E−02

Isolated rim analyses (February 2013)											
Egg6_spn_t3_2	Spinel	−27	−41.5	2.0	−44.8	4.2	−23.1	4.2	−23.4	5.5	6.45E−04
Egg6_spn_t3_3	Spinel	−21	−43.1	2.0	−48.6	4.2	−26.1	4.2	−26.4	5.5	1.45E−04
Interior (December 2012)											
Egg6_fass1	Vein grossular	Interior	0.2	1.8	−0.7	3.3	−0.8	3.4	0.5	5.1	3.09E−02
Egg6_fass2	Fassaite	Interior	−45.5	1.8	−43.2	2.9	−19.5	3.1	−20.2	4.9	3.19E−02
Egg6_fass3_1	Vein grossular	Interior	5.9	1.8	1.2	3.5	−1.9	3.6	−0.6	5.2	2.58E−02
Representative analyses in Melilite margin (February 2013)											
Egg6_spn_mantle_4	Spinel	60	−42.1	1.8	−47.6	3.7	−25.7	3.7	−26.0	5.2	7.93E−06
Egg6_spn_mantle_2	Spinel	144	−39.2	1.8	−45.3	3.7	−24.9	3.7	−25.2	5.2	6.21E−06
Egg6_spn_mantle_3	Spinel	175	−43.0	1.9	−50.6	3.9	−28.2	3.9	−28.5	5.3	4.11E−06
Egg6_spn_mantle_1	Spinel	467	−41.5	1.8	−48.9	3.7	−27.2	3.7	−27.5	5.2	6.69E−06
Egg6_fs_mantle_1	Fassaite	1056	−29.6	1.6	−32.3	3.4	−16.9	3.5	−17.2	5.3	3.66E−02
Egg6_fs_mantle_2	Fassaite	1432	−33.1	1.7	−34.8	3.8	−17.5	3.8	−17.8	5.5	2.94E−02
Representative analyses in core (Feburary-March 2013)											
Egg6_spn_core_4	Spinel	2065	−42.0	1.9	−47.2	4.0	−25.3	4.0	−25.6	5.4	1.38E−08
Egg6_spn_core_3	Spinel	2452	−43.7	2.0	−44.8	4.1	−22.0	4.1	−22.3	5.4	1.13E−08
Egg6_spn_core_2	Spinel	2733	−45.0	1.8	−48.6	3.6	−25.2	3.6	−25.5	5.1	2.79E−08
Egg6_an_core_1	Anorthite	3026	2.9	1.6	−2.8	3.5	−4.3	3.5	−3.3	5.1	3.15E−02
Egg6_an_core_2	Anorthite	3167	−3.7	1.8	−13.1	3.9	−11.2	3.9	−10.2	5.4	2.84E−02
Egg6_spn_core_1	Spinel	3202	−39.8	1.9	−42.6	3.9	−21.9	4.0	−22.2	5.3	8.47E−06

TS4 oxygen isotope data

Spot	Mineral	From edge of inclusion (μm)	$\delta^{18}O/^{16}O$*	2σ (‰)*	$\delta^{17}O/^{16}O$*	2σ (‰)*	$\Delta^{17}O$*	2σ (‰)*	$\Delta^{17}O$**	2σ (‰)**	$^{28}Si/^{16}O$
Traverse-1 (August 2011)											
TS4_WL_3	Olivine	−77	−6.3	1.5	−3.4	3.3	−0.2	3.4	0.7	5.0	8.97E−04
TS4_WL_4	Olivine	−71	−7.8	1.3	−5.2	2.4	−1.1	2.5	−0.2	4.5	8.79E−04
TS4_WL_5	Olivine	−67	−13.0	1.6	−11.9	3.1	−5.1	3.2	−4.2	4.8	6.66E−04
TS4_WL_6	Olivine	−60	−36.1	1.4	−40.0	3.0	−21.3	3.1	−20.4	4.8	8.18E−04
TS4_WL_7	Olivine	−53	−15.8	1.4	−19.9	3.0	−11.7	3.1	−10.8	4.8	8.41E−04
TS4_WL_8	Olivine	−46	−32.2	1.4	−35.9	3.0	−19.2	3.1	−18.2	4.8	8.83E−04
TS4_WL_9	Olivine	−39	−6.0	1.6	−9.9	3.0	−6.8	3.2	−5.9	4.8	9.92E−04
TS4_WL_10	Al-pyroxene + <spinel	−33	0.8	1.5	−5.4	3.0	−5.8	3.1	−4.9	4.8	8.66E−04
TS4_interior_16	Spinel	0	−28.5	1.9	−34.8	2.8	−19.9	3.0	−20.1	4.8	8.27E−05
TS4_interior_17	Sodalite	7	12.1	1.8	8.6	3.4	2.3	3.5	0.8	4.8	7.14E−04
TS4_interior_18	Sodalite	14	8.5	1.7	2.3	3.2	−2.1	3.3	−3.6	4.6	7.49E−04
TS4_interior_19	Sodalite	20	8.9	1.7	3.1	3.4	−1.5	3.6	−3.0	4.8	6.11E−04
TS4_interior_20	Melilite	34	12.3	1.7	5.9	3.4	−0.5	3.5	−2.0	4.7	8.08E−04
TS4_interior_21	Melilite	43	13.1	1.7	7.5	3.3	0.7	3.4	−0.8	4.7	9.11E−04
TS4_interior_23	Spinel + fassaite	109	−30.7	2.0	−39.9	3.1	−23.9	3.3	−24.0	4.9	1.83E−04
TS4_interior_24	Fassaite + < spinel	143	−36.2	1.7	−41.3	3.2	−22.5	3.3	−21.6	4.9	9.64E−04
TS4_interior_25	Fassaite + spinel	189	−39.2	1.5	−45.4	3.1	−25.0	3.2	−24.1	4.9	7.63E−04
TS4_interior_26	Fassaite	226	−30.0	1.5	−34.8	3.0	−19.2	3.1	−18.3	4.8	9.96E−04
TS4_interior_27	Melilite	349	8.7	1.5	4.0	3.0	−0.6	3.1	−2.1	4.4	9.86E−04

(*continued on next page*)

Table 1 (*continued*)

Spot	Mineral	From edge of inclusion (μm)	$\delta^{18}O/^{16}O$*	2σ (‰)*	$\delta^{17}O/^{16}O$*	2σ (‰)*	$\Delta^{17}O$*	2σ (‰)*	$\Delta^{17}O$**	2σ (‰)**	$^{28}Si/^{16}O$
Traverse-2 (August 2011)											
TS4_mel_55	Olivine	−80	−13.1	1.3	−7.0	2.4	−0.2	2.5	0.7	4.4	1.67E−03
TS4_mel_52	Melilite	35	14.9	1.9	7.4	3.3	−0.4	3.4	−1.9	4.7	1.01E−03
TS4_mel_51	Melilite	44	13.8	1.7	6.1	3.1	−1.0	3.2	−2.5	4.5	1.07E−03
TS4_mel_50	Melilite	54	14.4	1.8	5.1	3.0	−2.4	3.1	−3.9	4.5	1.06E−03
TS4_mel_49	Melilite	64	7.8	1.5	2.3	2.9	−1.7	3.0	−3.2	4.3	8.70E−04
TS4_mel_48	Melilite	75	9.3	1.5	2.5	3.0	−2.4	3.1	−3.9	4.4	8.51E−04
TS4_mel_47	Melilite	85	−12.9	1.6	−7.6	3.3	−0.9	3.4	−2.5	4.7	1.18E−03
TS4_mel_45	Spinel	105	−43.0	2.0	−43.8	3.0	−21.4	3.2	−21.5	4.9	3.11E−05
TS4_mel_44	Melilite	115	12.8	1.8	7.5	3.1	0.9	3.3	−0.6	4.6	9.69E−04
TS4_mel_43	Melilite	125	12.7	1.5	5.2	2.7	−1.4	2.8	−2.9	4.3	1.02E−03
TS4_mel_42	Melilite	136	−0.4	1.7	0.4	3.3	0.6	3.4	−0.9	4.7	1.03E−03
TS4_mel_41	Melilite	144	12.8	1.9	6.4	3.1	−0.3	3.3	−1.8	4.6	9.81E−04
TS4_mel_40	Melilite	153	9.6	1.6	5.1	3.4	0.1	3.5	−1.4	4.7	1.05E−03
TS4_mel_39	Melilite	164	13.0	1.6	5.2	3.0	−1.5	3.1	−3.1	4.4	1.10E−03
TS4_mel_38	Spinel	174	−40.3	2.0	−41.8	3.1	−20.8	3.2	−20.9	4.9	4.17E−04
TS4_mel_37	Fassaite	185	−32.8	1.5	−38.3	3.1	−21.3	3.2	−20.4	4.9	9.60E−04
TS4_mel_36	Fassaite	194	−31.7	1.4	−38.6	2.8	−22.1	2.9	−21.2	4.7	1.03E−03
TS4_mel_35	Fassaite + <spinel	218	−43.8	1.6	−44.7	3.2	−21.9	3.3	−21.0	4.9	7.18E−06
TS4_mel_34	Melilite (some alteration)	246	15.9	1.9	11.2	3.1	2.9	3.2	1.4	4.5	1.16E−03
TS4_mel_32	Anorthite (some alteration)	318	12.2	1.8	6.1	3.6	−0.2	3.8	−1.7	4.9	7.91E−04
TS4_mel_31	Spinel	467	−32.0	2.2	−38.0	3.2	−21.4	3.4	−21.5	5.0	7.16E−06
TS4_mel_30	Melilite	614	7.9	1.6	−0.8	3.2	−4.9	3.3	−6.4	4.6	1.04E−03
TS4_mel_29	Spinel	769	−33.3	1.9	−40.9	3.1	−23.6	3.3	−23.7	4.9	7.29E−06
TS4_mel_28	Anorthite	896	−8.8	1.6	−15.0	3.2	−10.5	3.3	−12.0	4.6	8.27E−04
Assorted interior spots (August 2011)											
TS4_lgfass_1	Fassaite	880	−33.7	1.6	−41.6	3.0	−24.1	3.1	−25.5	4.8	1.05E−03
TS4_lgfass_2	Fassaite	880	−33.1	1.6	−38.4	3.3	−21.2	3.4	−22.6	5.0	1.05E−03
TS4_lgfass_3	Fassaite	880	−35.5	1.6	−40.0	3.3	−21.6	3.5	−22.9	5.0	1.03E−03
TS4_pal_fs_1	Fassaite	960	−33.6	1.7	−40.2	3.3	−22.7	3.4	−24.1	5.0	1.05E−03
TS4_pal_fs_2	Fassaite	965	−34.9	1.6	−39.3	3.5	−21.2	3.6	−22.6	5.1	1.12E−03
TS4_pal_fs_3	Fassaite	970	−33.2	1.7	−40.1	3.2	−22.8	3.3	−24.2	4.9	1.06E−03
TS4_pal_an_1	Anorthite	910	0.7	1.8	−7.0	3.9	−7.4	4.0	−8.8	5.1	8.21E−04
TS4_pal_an_2	Anorthite	915	1.7	2.0	−7.4	3.9	−8.3	4.0	−9.7	5.1	8.30E−04
TS4_pal_an_3	Anorthite	920	2.3	1.8	−1.4	3.7	−2.6	3.8	−4.0	5.0	8.49E−04
TS4_pal_mel_1	Melilite	930	6.5	1.8	−1.4	3.6	−4.8	3.7	−6.1	4.9	8.47E−04
TS4_pal_mel_2	Melilite	935	4.0	1.7	−1.8	3.6	−3.8	3.7	−5.2	4.9	1.06E−03
TS4_pal_sp_1	Spinel	940	−32.3	2.2	−38.2	3.7	−21.4	3.9	−21.8	5.3	6.97E−06
TS4_pal_sp_2	Spinel	945	−29.4	2.1	−41.6	3.8	−26.3	3.9	−26.7	5.4	1.07E−04
TS4_pal_sp_3	Spinel	950	−36.7	2.2	−41.4	3.7	−22.3	3.9	−22.8	5.4	1.05E−05
Internal inclusion (August 2011)											
TS4_dark_1	Pyroxene		11.9	1.7	1.5	3.6	−4.7	3.7	−3.8	5.2	1.19E−03

TS4_bright_1	Pyroxene (Fe)	14.8	1.6	6.4	3.3	−1.3	3.4	−0.4	5.0	1.04E−03
TS4_olint_1	Olivine	−3.0	1.8	−6.2	3.4	−4.6	3.5	−3.7	5.1	9.53E−04
TS4_olrim_1	Olivine	9.8	1.6	4.3	3.2	−0.8	3.3	0.1	4.9	1.36E−03
TS4_sp_1	Spinel	−35.2	2.0	−41.9	3.5	−23.6	3.7	−24.0	5.2	6.77E−06
TS4_sp_2	Spinel	−31.0	2.1	−40.6	3.4	−24.5	3.6	−24.9	5.2	5.32E−06
TS4_mel_3	Spinel + melilite	−27.9	2.1	−37.9	3.3	−23.4	3.5	−23.8	5.1	1.68E−04
TS4_mel_4	Unknown Fe–Mg silicate	−8.6	2.7	−5.7	5.0	−1.3	5.2	−0.4	6.4	1.35E−03
TS4_ol_2	Olivine	−4.2	1.7	−9.8	3.8	−7.6	3.9	−6.7	5.4	9.45E−04
TS4_ol_3	Olivine	−4.8	1.7	−11.8	3.9	−9.3	4.0	−8.3	5.4	1.01E−03

L6 oxygen isotope data

Spot	Mineral	From edge of inclusion (μm)	$\delta^{18}O/^{16}O$*	2σ (‰)*	$\delta^{17}O/^{16}O$*	2σ (‰)*	$\Delta^{17}O$*	2σ (‰)*	$\Delta^{17}O$**	2σ (‰)**	$^{28}Si/^{16}O$
Traverse 2 (March 2013)											
L6_t2@1_1	Melilite + <spinel	−47.4	−21.3	1.7	−23.2	4.3	−12.0	4.4	−11.0	5.8	1.90E−02
L6_t2@1_2	Spinel	−3.6	−42.4	2.0	−46.7	4.1	−24.6	4.2	−24.9	5.5	1.41E−04
L6_t2@1_4	Melilite + <spinel	26.6	7.2	1.9	−1.1	3.9	−4.8	4.0	−3.8	5.5	2.19E−02
L6_t2@1_5	Melilite	41.1	3.3	2.0	−3.7	4.3	−5.5	4.4	−4.4	5.8	2.05E−02
L6_t2@1_6	Melilite	57.0	7.6	1.7	−1.8	3.8	−5.8	3.9	−4.7	5.4	2.11E−02
L6_t2@1_7	Melilite	72.3	4.5	1.7	−3.9	3.9	−6.2	4.0	−5.2	5.5	2.16E−02
L6_t2@1_9	Melilite	104.0	7.5	1.8	0.8	3.8	−3.1	3.9	−2.1	5.4	2.13E−02
L6_t2@1_10	Melilite	119.8	6.3	1.8	−1.8	4.0	−5.1	4.1	−4.1	5.5	2.21E−02
L6_t2@1_11	Melilite	135.6	4.3	1.7	−3.9	4.0	−6.2	4.1	−5.1	5.6	2.19E−02
L6_t2@1_12	Melilite	152.4	7.0	1.8	−5.5	4.1	−9.1	4.2	−8.1	5.7	2.23E−02
L6_t2@1_13	Melilite	168.0	2.8	1.8	−7.5	4.1	−9.0	4.2	−7.9	5.6	2.32E−02
L6_t2@1_14	Melilite	183.8	2.8	1.9	−5.2	4.2	−6.6	4.3	−5.6	5.7	2.28E−02
L6_t2@1_15	Melilite	198.9	5.4	1.9	−5.3	4.0	−8.1	4.1	−7.1	5.6	2.16E−02
L6_t2@1_16	Melilite	215.4	7.7	1.9	−0.7	3.7	−4.7	3.8	−3.7	5.4	2.32E−02
L6_t2@1_17	Melilite	230.8	4.1	1.9	−7.9	4.1	−10.1	4.2	−9.1	5.7	2.30E−02
L6_t2@1_18	Melilite	246.8	2.0	2.0	−4.9	4.3	−5.9	4.4	−4.9	5.8	2.26E−02
L6_t2@1_19	Melilite	262.7	1.1	1.8	−7.7	3.9	−8.3	4.0	−7.3	5.5	2.38E−02
L6_t2@1_20	Melilite	278.9	4.5	1.9	−3.4	4.2	−5.7	4.3	−4.7	5.7	2.45E−02
L6_t2@1_21	Melilite	294.1	4.1	1.7	−3.1	4.0	−5.2	4.1	−4.2	5.5	2.31E−02
L6_t2@1_22	Melilite	310.2	3.3	1.9	−4.3	4.0	−6.0	4.1	−5.0	5.5	2.33E−02
L6_t2@1_24	Melilite	341.2	2.7	1.8	−6.7	4.1	−8.1	4.2	−7.1	5.6	2.24E−02
L6_t2@1_26	Melilite	373.0	9.8	1.9	0.2	4.4	−4.9	4.5	−3.9	5.8	2.11E−02
L6_t2@1_27	Melilite	387.6	9.7	1.9	3.7	4.1	−1.4	4.2	−0.4	5.6	2.20E−02
L6_t2@1_28	Melilite	403.4	5.1	1.9	−2.7	4.4	−5.4	4.5	−4.3	5.8	2.27E−02
L6_t2@1_29	Melilite	418.6	5.5	1.8	−7.2	3.8	−10.0	3.9	−9.0	5.4	2.25E−02
L6_t2@1_30	Melilite	434.0	6.0	1.8	−5.4	3.6	−8.5	3.8	−7.5	5.3	2.30E−02
Traverse 4 (March 2013)											
L6_t4_1@1_1	Melilite ± ti pyroxene	−208.8	−40.0	1.8	−39.8	3.6	−19.0	3.7	−18.0	5.2	2.17E−02
L6_t4_1@1_2	Melilite	−193.6	4.7	1.9	−3.9	4.1	−6.4	4.2	−5.4	5.6	1.82E−02
L6_t4_1@1_3	Melilite ± spinel?	−179.2	−46.8	1.7	−51.0	3.5	−26.6	3.6	−25.6	5.2	2.02E−02
L6_t4_1@1_4	Melilite	−164.0	−12.7	1.9	−18.7	3.9	−12.0	4.0	−11.0	5.5	1.74E−02
L6_t4_1@1_5	Melilite	−147.5	−23.7	1.9	−29.2	3.7	−16.9	3.8	−15.9	5.4	2.17E−02
L6_t4_1@1_6	Melilite	−132.0	−12.0	1.8	−21.9	3.9	−15.6	4.0	−14.6	5.5	1.91E−02
L6_t4_1@1_7	Melilite + spinel	−117.2	8.3	2.0	−1.4	4.2	−5.8	4.3	−4.7	5.7	1.63E−02

(*continued on next page*)

Table 1 (*continued*)

Spot	Mineral	From edge of inclusion (μm)	$\delta^{18}O/^{16}O$*	2σ (‰)*	$\delta^{17}O/^{16}O$*	2σ (‰)*	$\Delta^{17}O$*	2σ (‰)*	$\Delta^{17}O$**	2σ (‰)**	$^{28}Si/^{16}O$
L6_t4_1@1_10	Spinel	−81.2	−40.1	2.0	−45.3	3.9	−24.4	4.1	−24.7	5.7	8.34E−04
L6_t4_1@1_11	Ti pyx	−71.8	−16.2	1.5	−20.0	3.3	−11.5	3.4	−11.8	5.3	2.94E−02
L6_t4_1@1_12	Melilite	−61.1	5.8	1.9	−2.3	3.9	−5.3	4.1	−4.3	5.5	2.07E−02
L6_t4_1@1_13	Melilite	−52.1	7.2	1.8	−0.9	3.7	−4.6	3.9	−3.6	5.4	2.07E−02
L6_t4_1@1_14	Spinel	−29.7	−41.8	2.1	−45.6	4.1	−23.9	4.2	−24.1	5.5	5.92E−05
L6_t4_1@1_15	Spinel	−0.2	−41.9	2.0	−46.9	4.5	−25.0	4.6	−25.3	5.8	3.09E−05
Traverse 1 (March 2013)											
L6_t1@1_1	Melilite	−48.0	4.4	2.0	−3.0	3.8	−5.4	3.9	−4.3	5.4	2.10E−02
L6_t1@1_2	Low Ti pyx	−33.6	−12.8	2.0	−15.3	4.0	−8.6	4.1	−8.9	5.8	1.53E−02
L6_t1@1_4	Melilite	14.5	−8.4	1.7	−14.0	3.8	−9.6	3.9	−8.6	5.4	2.16E−02
L6_t1@1_5	Spinel	29.4	−38.6	2.1	−42.7	4.4	−22.6	4.5	−22.8	5.8	2.69E−04
L6_t1@1_6	Melilite	43.8	−4.6	1.9	−13.8	3.8	−11.4	3.9	−10.4	5.4	1.98E−02
L6_t1@1_7	Melilite	59.3	−4.8	1.7	−13.0	3.9	−10.4	4.0	−9.4	5.4	2.05E−02
L6_t1@1_10	Melilite	104.7	8.2	1.9	0.7	4.0	−3.5	4.2	−2.5	5.6	2.13E−02
L6_t1@1_11	Melilite	119.9	7.9	1.9	1.1	3.7	−3.0	3.9	−2.0	5.4	2.37E−02
L6_t1@1_12	Melilite	134.9	5.6	1.9	−1.3	3.9	−4.2	4.0	−3.2	5.5	2.24E−02
L6_t1@1_13	Melilite	149.6	6.4	1.8	0.6	4.1	−2.7	4.2	−1.7	5.6	2.29E−02
L6_t1@1_14	Melilite	165.0	5.4	1.8	−3.2	4.1	−6.0	4.2	−5.0	5.6	2.38E−02
L6_t1@1_15	Melilite	180.5	5.5	2.0	−3.7	4.1	−6.6	4.2	−5.6	5.7	2.34E−02
Traverse 3 (March 2013)											
L6_t3@1_1	Ti pyx	−71.9	−20.0	1.6	−23.6	3.5	−13.1	3.5	−13.4	5.4	2.45E−02
L6_t3@1_2	Spinel	−32.4	−38.7	1.8	−46.6	4.0	−26.4	4.1	−26.7	5.4	1.11E−04
L6_t3@1_3	Spinel	−22.9	−43.4	1.9	−47.8	4.0	−25.2	4.1	−25.5	5.4	2.11E−05
L6_t3@1_4	Spinel	−13.0	−41.4	2.1	−47.3	4.1	−25.7	4.3	−26.0	5.6	9.27E−05
L6_t3@1_5	Spinel	−2.9	−40.3	2.2	−47.6	3.8	−26.6	4.0	−26.9	5.4	2.43E−05
L6_t3@1_6	Spinel	0.0	−42.3	2.1	−44.3	4.2	−22.3	4.3	−22.5	5.6	2.07E−04
L6_t3@1_7	Melilite	1.1	−40.1	1.9	−40.7	3.9	−19.8	4.0	−18.8	5.5	1.95E−02
L6_t3@1_8	Melilite	4.7	−14.3	1.9	−21.5	4.2	−14.1	4.3	−13.0	5.7	1.93E−02
L6_t3@1_9	Melilite	10.2	−16.3	1.8	−29.3	4.1	−20.8	4.2	−19.8	5.6	1.97E−02
L6_t3@1_10	Melilite	17.1	−10.0	1.8	−18.2	3.6	−13.0	3.7	−12.0	5.3	2.05E−02
L6_t3@1_11	Melilite	25.4	−12.1	1.9	−15.5	3.9	−9.2	4.0	−8.2	5.5	2.02E−02
L6_t3@1_12	Spinel + <melilite	33.9	−31.6	2.1	−41.8	4.5	−25.4	4.6	−25.6	5.8	5.20E−03
L6_t3@1_13	Melilite	42.8	−13.9	1.7	−19.6	4.0	−12.4	4.1	−11.4	5.5	1.93E−02
L6_t3@1_14	Melilite	51.5	−4.0	1.8	−10.5	3.7	−8.4	3.8	−7.4	5.3	2.08E−02
L6_t3@1_15	Melilite	61.6	−4.6	1.8	−13.0	4.0	−10.6	4.1	−9.6	5.5	2.05E−02
3Jan_L6_B_1	Ti pyx + sp?	−189.9	−2.5	2.1	−7.2	3.4	−3.2	3.3			1.53E−02
Pyroxene (January 2014)											
L6_2	Diopside	−247.1	−51.9	2.0	−48.6	3.2	−21.5	3.3	−20.3	4.7	3.62E−02
L6_3	Ti pyx	−238.1	−38.9	2.0	−37.6	3.1	−17.4	3.3	−16.1	4.7	2.14E−02
L6_4	Ti pyx	−241.1	−42.6	2.4	−36.5	3.3	−14.3	3.5	−13.0	4.8	1.77E−02
L6_5	Diopside	−245.0	−24.7	2.5	−26.4	3.6	−13.5	3.9	−12.3	5.1	3.64E−02
L6_7	Diopside	−243.0	−46.5	1.9	−44.8	3.2	−20.6	3.3	−19.3	4.7	3.72E−02

L6_8	Diopside	−249.4	−39.5	2.0	−38.2	3.3	−17.6	3.4	−16.3	4.8	3.78E−02
ALH3 oxygen isotope data											
Spot	Mineral	From edge of inclusion (μm)	$\delta^{18}O/^{16}O$*	2σ (‰)*	$\delta^{17}O/^{16}O$*	2σ (‰)*	$\Delta^{17}O$*	2σ (‰)*	$\Delta^{17}O$**	2σ (‰)**	$^{28}Si/^{16}O$
Traverse 4 (December 2012)											
ALH3_t4_1	Olivine	−81	−12.8	1.6	−17.2	2.6	−10.6	2.8	−11.3	4.7	2.32E−02
ALH3_t4_2	Olivine	−73	−0.2	1.7	0.2	2.5	0.3	2.7	−0.4	4.6	2.19E−02
ALH3_t4_3	Al-pyroxene	−64	−5.2	1.7	−11.3	2.8	−8.6	3.0	−9.3	4.8	3.65E−02
ALH3_t4_4	Ti-pyroxene	−53	−14.4	1.8	−18.9	3.2	−11.4	3.4	−12.1	5.1	1.58E−02
ALH3_t4_5	Ti pyroxene	−39	−37.8	1.7	−34.7	3.1	−15.0	3.2	−15.8	5.0	9.16E−03
ALH3_t4_6	Spinel on crack	−5	−43.6	1.3	−46.4	2.9	−23.7	3.0	−24.4	5.0	1.39E−03
ALH3_t4_7	Plagioclase on crack	4	−8.8	1.8	−1.8	3.2	2.8	3.3	4.1	5.0	3.47E−02
ALH3_t4_8a	Plagioclase on crack	14	−13.2	1.5	−6.6	2.9	0.3	3.0	1.6	4.8	6.38E−02
ALH3_t4_9	Melilite	24	5.1	1.9	−2.8	3.2	−5.4	3.3	−4.1	5.0	2.18E−02
ALH3_t4_10	Melilite	33	1.9	1.7	−6.8	3.2	−7.7	3.3	−6.4	5.0	2.29E−02
ALH3_t4_11	Melilite	42	−3.9	1.7	−10.4	2.9	−8.4	3.1	−7.1	4.9	2.12E−02
ALH3_t4_12	Melilite	52	−1.9	1.9	−10.3	3.3	−9.3	3.5	−8.0	5.1	1.89E−02
ALH3_t4@1_1	Melilite	70	−0.9	1.7	−8.1	3.0	−7.7	3.1	−6.4	4.9	2.20E−02
ALH3_t4@1_2	Melilite	89	−1.2	1.7	−8.4	3.4	−7.8	3.5	−6.5	5.1	2.00E−02
ALH3_t4@1_3	Melilite	110	3.7	1.7	−4.5	3.0	−6.5	3.2	−5.2	4.9	2.03E−02
ALH3_t4@1_4	Melilite + grossular	129	3.8	1.9	0.6	3.8	−1.4	3.9	−0.1	5.5	2.45E−02
ALH3_t4@1_5	Melilite	149	3.0	1.7	−5.5	3.1	−7.1	3.2	−5.8	5.0	2.11E−02
ALH3_t4@1_6	Melilite	169	1.6	1.7	−5.5	3.2	−6.4	3.3	−5.1	5.0	2.05E−02
ALH3_t4@1_7	Melilite	189	4.2	1.7	−3.5	3.3	−5.7	3.4	−4.4	5.1	2.20E−02
ALH3_t4@1_8	Melilite	209	3.9	1.8	−0.9	3.3	−2.9	3.4	−1.6	5.1	2.02E−02
ALH3_t4@1_9	Melilite	228	2.9	1.8	−2.7	3.3	−4.2	3.4	−2.9	5.1	2.56E−02
ALH3_t4@1_10	Melilite	248	14.4	1.8	3.6	3.1	−3.9	3.2	−2.6	5.0	3.17E−02
Traverse 3 (December 2012)		From edge of inclusion									
ALH3_t3_1a	Olivine	−75	−52.2	1.5	−52.9	2.4	−25.7	2.5	−27.8	4.8	2.39E−02
ALH3_t3_2a	Olivine	−66	−46.9	1.5	−49.6	2.4	−25.1	2.6	−27.2	4.8	2.54E−02
ALH3_t3_3a	Al-pyroxene	−56	−19.2	1.7	−21.1	3.0	−11.1	3.4	−13.5	5.1	3.85E−02
ALH3_t3_4	Ti-pyroxene	−45	−15.6	1.8	−15.4	3.1	−7.3	3.1	−8.4	5.1	2.22E−02
ALH3_t3_5	Grossular	−39	5.2	1.8	−0.6	3.5	−3.3	3.6	−3.3	5.4	2.41E−02
ALH3_t3_6	Spinel + grossular	−2	−27.6	1.5	−30.0	3.0	−15.6	3.1	−17.7	5.2	1.05E−02
ALH3_t3_3	Spinel	0	−47.9	1.1	−49.2	2.4	−24.2	2.4	−24.4	4.6	3.49E−04
Near Traverse 3 near edge (December 2012)		From edge of inclusion									
ALH3_t3_1	Melilite	35	−5.2	1.7	−12.4	2.9	−9.7	3.0	−8.4	4.8	2.57E−02
ALH3_t3_2	Melilite	45	−6.1	1.5	−9.5	2.9	−6.3	3.0	−5.1	4.8	3.41E−02
Traverse 2 at edge of inner pocket (December 2012)		From edge of pocket									
ALH3_t2_1	Andradite	−65	−8.1	1.5	−5.4	2.2	−1.2	2.3	−1.9	4.4	4.04E−02
ALH3_t2_2	Al-pyroxene	−49	−41.6	1.7	−42.7	3.0	−21.0	3.1	−22.1	4.9	3.64E−02
ALH3_t2_3	Al-pyroxene	−38	−3.2	1.6	−5.6	2.7	−4.0	2.9	−5.0	4.7	3.69E-02

(*continued on next page*)

Table 1 (*continued*)

Spot	Mineral	From edge of inclusion (μm)	$\delta^{18}O/^{16}O$*	2σ (‰)*	$\delta^{17}O/^{16}O$*	2σ (‰)*	$\Delta^{17}O$*	2σ (‰)*	$\Delta^{17}O$**	2σ (‰)**	$^{28}Si/^{16}O$
ALH3_t2_4	Spinel	−18	−44.8	1.3	−42.4	3.0	−19.1	3.1	−19.8	5.1	1.58E−05
ALH3_t2_5	Spinel	−10	−40.2	1.3	−44.3	2.9	−23.3	3.0	−24.1	5.0	5.70E−05
ALH3_t2_6	Melilite ± spl	7	−16.1	1.6	−18.5	2.9	−10.1	3.0	−8.8	4.8	2.44E−02
ALH3_t2_7	Melilite	21	−10.2	1.6	−13.1	3.1	−7.8	3.2	−6.5	4.9	2.34E−02
Traverse 1 at edge of inner pocket (December 2012)		From edge of pocket									
ALH3_t1_1	Andradite	−65	10.1	1.7	1.9	3.1	−3.4	3.2	−4.1	5.0	2.76E−02
ALH3_t1_2	Al-pyroxene	−51	−2.4	1.8	−7.9	3.0	−6.6	3.2	−7.4	4.9	2.81E−02
ALH3_t1_3	Ti-pyroxene	−42	−16.1	1.9	−15.7	3.7	−7.3	3.8	−8.0	5.4	1.64E−02
ALH3_t1_4	Spinel	−34	−43.3	1.4	−44.5	3.1	−21.9	3.2	−22.6	5.1	1.95E−05
ALH3_t1_5	Spinel	−21	−43.9	1.5	−43.0	3.3	−20.2	3.4	−20.9	5.2	9.99E−05
ALH3_t1_6	Spinel	−10	−41.9	1.4	−43.3	3.3	−21.5	3.4	−22.2	5.3	5.76E−05
ALH3_t1_7	Spinel + melilite > perovskite	0	−27.7	1.3	−31.8	2.8	−17.3	2.9	−18.1	5.0	4.71E−05
ALH3_t1_8	Melilite	11	−7.6	1.7	−15.0	3.3	−11.0	3.4	−9.7	5.1	1.95E−02

Ef-1 oxygen isotope data

Spot	Mineral	From edge of inclusion (μm)	$\delta^{18}O/^{16}O$*	2σ (‰)*	$\delta^{17}O/^{16}O$*	2σ (‰)*	$\Delta^{17}O$*	2σ (‰)*	$\Delta^{17}O$**	2σ (‰)**	$^{28}Si/^{16}O$
Traverse-1 (August 2011)											
EF_matrix_2	Olivine matrix	−3	10.9	1.6	6.6	3.6	0.9	3.7	1.8	5.2	1.18E−03
EF_matrix_3	Olivine matrix	−3	8.5	1.7	0.0	3.3	−4.4	3.4	−3.5	5.0	1.18E−03
EF_matrix_4	Olivine matrix	−3	6.4	1.9	1.0	3.7	−2.3	3.8	−1.5	5.2	1.16E−03
EF_WL_7	Spinel	−3	−30.8	2.2	−35.8	3.5	−19.7	3.6	−19.8	5.2	5.12E−04
EF_WL_8	Spinel + diopside	−3	−44.1	2.4	−46.3	4.3	−23.3	4.5	−23.4	5.8	2.46E−04
EF_WL_9	Spinel + ≪melilite	−3	−39.5	2.4	−41.5	4.2	−21.0	4.3	−21.1	5.7	2.78E−05
EF_interior_1	Melilite	Interior margin	5.1	2.0	−1.1	3.9	−3.7	4.0	−5.3	5.2	8.80E−04
Traverse-2 (August 2011)											
EF_matrix_13	Olivine matrix	−21	6.0	1.6	2.7	3.3	−0.4	3.5	0.5	5.0	1.21E−03
EF_WL_12	Ti pyroxene	−15	−44.8	1.8	−43.8	3.7	−20.5	3.8	−19.6	5.3	1.31E−03
EF_WL_11	Ti pyroxene	−9	−25.9	1.7	−25.0	3.5	−11.5	3.7	−10.6	5.2	1.23E−03
EF_WL_14	Spinel	−2	−35.3	2.1	−40.1	3.4	−21.7	3.6	−21.8	5.1	2.19E−05
EF_interior_15	Melilite	5	−21.2	1.8	−16.6	4.2	−5.6	4.3	−7.1	5.3	9.65E−04
EF_interior_17	Melilite	15	−8.5	1.9	−10.5	3.5	−6.1	3.6	−7.7	4.8	9.15E−04
EF_interior_18	Melilite	21	−18.3	1.9	−14.4	3.9	−4.9	4.0	−6.4	5.1	9.08E−04
EF_interior_19	Melilite	28	−0.7	1.9	−7.6	3.5	−7.3	3.6	−8.8	4.8	1.27E−03
EF_interior_20	Melilite	34	−13.9	2.1	−12.0	3.5	−4.8	3.7	−6.3	4.9	1.03E−03
EF_interior_21	Melilite	40	1.5	1.9	−0.3	3.4	−1.1	3.6	−2.6	4.8	1.47E−03
EF_interior_22	Melilite	52	−11.3	2.1	−12.2	4.3	−6.3	4.5	−7.8	5.5	1.41E−03
EF_interior_23	Melilite	68	−2.9	2.6	−5.4	4.5	−3.9	4.7	−5.5	5.7	1.70E−03
EF_interior_26	Melilite	93	−1.8	2.0	−3.6	4.3	−2.7	4.4	−4.2	5.5	1.48E−03
EF_interior_27	Melilite	111	−6.6	1.9	−4.9	3.5	−1.5	3.6	−3.0	4.8	1.47E−03

EF_interior_28	Melilite	131	−6.1	2.7	−6.0	4.3	−2.8	4.5	−4.3	5.5	1.26E−03
EF_interior_29	Melilite	161	4.8	2.0	0.5	3.7	−2.0	3.8	−3.5	5.0	1.51E−03
EF_interior_25	Spinel	179	−39.7	2.1	−41.7	3.7	−21.0	3.9	−21.1	5.4	8.24E−06
EF_interior_30	Melilite	192	6.4	2.4	3.6	4.3	0.3	4.5	−1.3	5.5	1.51E−03
EF_interior_32	Melilite	264	6.4	1.9	0.8	3.6	−2.5	3.7	−4.0	4.9	1.52E−03

* Standard mineral-specific instrumental corrections applied to measurements (i.e., olivine, anorthite, or spinel). Uncertainties include propagation of measured 2 se counting statistics and 2 se systematic errors of the mean for each mineral standard. These data are plotted in Figs. 9 and 10.

** Average standard mineral instrumental corrections applied to measurements. Uncertainties reflect the propogation of measured 2 se counting statistics and 2 sd scatter about the mean derived from all mineral standard measurements.

using backscattered electron and X-ray images) allowed confirmation of the phases analyzed, which is critical for interpretation of analyses within the fine mineral layers of WL rims and near crystal boundaries in interiors of CAIs. A normal-incidence electron gun was utilized for charge compensation.

Oxygen isotopic zoning profiles were obtained by conducting NanoSIMS traverses across the rims and outer margins of CAIs. In most cases more than one traverse across a comparable region of a given CAI was measured. Within select traverses, analyses were made out of spatial sequence in order to separate potential analytical shifts from gradients in the samples themselves. Measurements were made on six CAIs and include analyses of primary melilite, spinel, fassaite and anorthite; secondary grossular, plagioclase, and sodalite in the CAI interiors; and olivine, Ti-pyroxene, aluminous pyroxene, spinel, anorthite, hibonite, perovskite and secondary nepheline and andradite in the WL rims. Each individual datum reflects a $\sim 2 \times 2$ μm rastered spot analysis from a single mineral phase, as evaluated by the observed $^{28\ (or\ 30)}Si^-/^{16}O^-$ ion ratios and by SEM analyses after the NanoSIMS measurements, unless stated otherwise. Oxygen isotopic compositions are reported in terms of $\delta^{17}O$ and $\delta^{18}O$, the permil differences from the reference ratios of standard mean ocean water (SMOW); $\delta^i O = 10^3 \times (({}^iO/{}^{16}O)/({}^iO/{}^{16}O)_{SMOW} - 1)$, where i is either 17 or 18. $\Delta^{17}O$, defined as $\Delta^{17}O = \delta^{17}O - (0.521 \times \delta^{18}O)$, represents the departure of the sample composition from the terrestrial mass fractionation (TMF) line that defines the terrestrial oxygen reservoir.

Instrumental mass fractionation (IMF) and experimental reproducibility were determined through replicate analyses of terrestrial spinel, anorthite, grossular, pyroxene, and forsterite standards. The standard analyses were interspersed with unknowns. Periodically an automated series of standard analyses ($n \approx 10$–15) were run overnight. The individual measurements that made up these standard series scattered about their average value, but did not exhibit significant systematic shifts attesting to the fact that on a day-to-day timeframe instrument IMF conditions were stable. Over the ~3-year period of the study, however, IMF conditions did vary and data were corrected accordingly. The IMF corrections were handled in two different ways. In the first, mineral-specific corrections were applied to the unknown measurements based on the standards used for each session. In the second an average of the mineral-specific corrections was applied, based on the standards used for each session. The overall difference between the two approaches was negligible and only varied up to ~1.5‰ (see columns #8 and #10, respectively in Table 1 and details in Appendix II). Systematic mass independent effects varied among the different mineral standards in each analytical session, but by no more than ~2‰. The reproducibility in $\Delta^{17}O$ among 521 terrestrial mineral standard analyses was ⩽6‰ (2 sd), after IMF corrections were applied, and within a given session it was ~4‰ (2 sd) as summarized in Appendix II. For internal consistency only the spinel, anorthite, and olivine standards were used in the reported error of the unknowns as these were measured in every session. The uncertainty of individual

measurements was ⩽4‰ (2 sd) for $\delta^{17}O$ and ⩽2‰ (2 sd) for $\delta^{18}O$. In ideal cases (e.g., comparing the averages of multiple analyses of distinct regions along a single traverse within a given session), a difference in $\Delta^{17}O$ as small as ~1–2‰ (2 se) appears resolvable, whereas a more conservative evaluation of uncertainty consistent with the inter-session reproducibility of standards is closer to ±4‰ (2 sd).

2.1.1. Avoiding oxygen isotopic measurements of mineral mixtures

Analysis of more than one, isotopically-distinct, mineral phase in a single rastered spot may lead to spurious O-isotope values. This problem is particularly acute for the analysis of mineral layers within WL-rims, where the thin individual mineral layers can be difficult to resolve. We evaluated each O-isotope analysis for the possibility that it might reflect a mixture of two or more minerals by both comparing pre-analysis and post-analysis SEM images and evaluating the corresponding ^{28} or $^{30}Si^-/^{16}O^-$ ion ratios. This combined approach effectively identifies analytical volumes that sampled more than one mineral, as SEM images alone do not always reveal accessory phases or minor contributions. In general, the ^{28} or $^{30}Si^-/^{16}O^-$ ion ratios of individual minerals are diagnostic, especially between oxides and silicates in the present samples (Fig. 1). The ^{28} or $^{30}Si^-/^{16}O^-$ ratio of diopside is clearly distinguishable from that of melilite. It is not always possible, however, to use the ion ratio approach to distinguish Ti-pyroxene from a mixture of Ti-pyroxene and melilite, so the post-analysis SEM images were heavily relied upon. Among the samples analyzed here, only the WL rim on the Leoville sample (L6) has pyroxene in contact with melilite. Measurements of ^{28} or $^{30}Si^-/^{16}O^-$ ratios were not calibrated, and only intra-mount and intra-analytical session comparisons were made.

2.2. X-ray mapping and mineral compositions by scanning electron microscope and microprobe

Mineral compositions, X-ray maps and backscattered electron images (BEI) were obtained at NASA Johnson Space Center (JSC), The University of Chicago, and LLNL to study the petrography of the inclusions, guide NanoSIMS traverses, and verify the mineralogy of analysis spots. High-resolution BEI and digital X-ray maps were obtained with a JEOL JSM-7600F SEM at JSC and with an FEI Inspect F field emission SEM at LLNL. At JSC, X-ray maps were obtained with a ThermoElectron SDD X-ray detector and ThermoElectron software using a 15 kV beam and 30 nA beam current. At LLNL, element maps were made with an EDAX Apollo 40 energy-dispersive X-ray microanalysis system. At The University of Chicago, selected areas of the samples were documented with a JEOL JSM-5800LV SEM operated at 15 kV and 1 nA beam current.

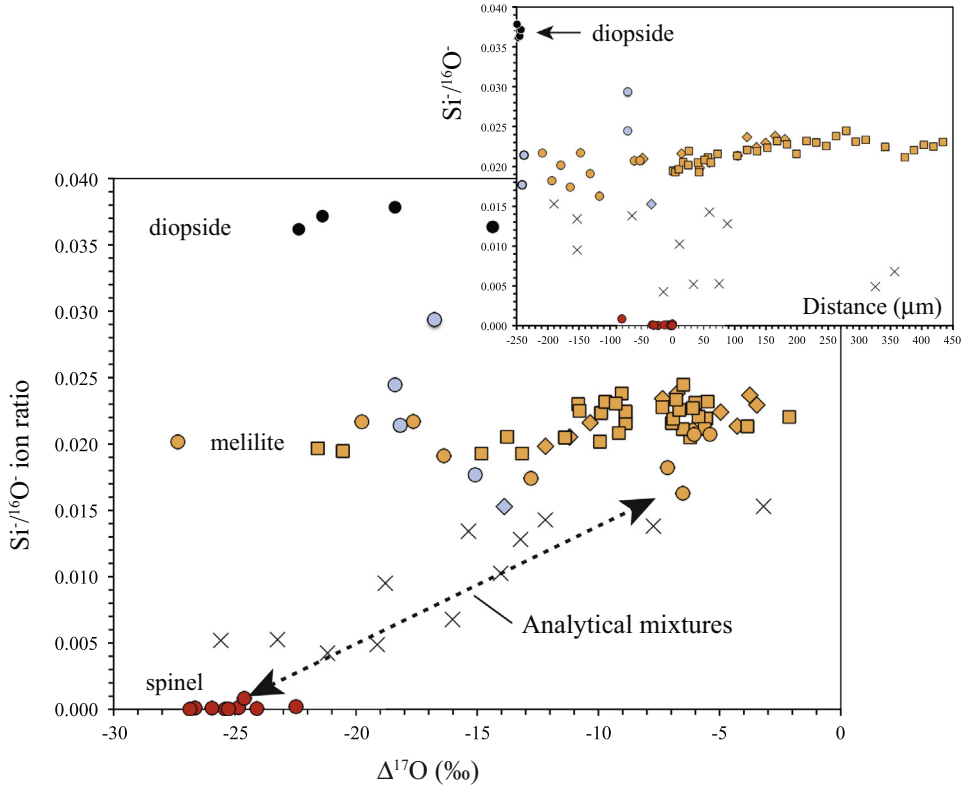

Fig. 1. $Si^-/^{16}O^-$ ion ratios from Leoville L6, showing that this ratio can be used to distinguish mixtures of two or more phases from pure phases. Inset shows systematic shifts in the $Si^-/^{16}O^-$ ion ratio at the outer margin of the inclusion related to melilite chemical composition zoning. Filled symbols are pure phases: spinel (red), melilite (tan), Ti-pyroxene (light blue), diopside (black); mixtures shown by x's. Symbols of the same color, but different shape (i.e., circle, square, and diamond) indicate the same mineral phase analyzed in different NanoSIMS transects. (For interpretation of the references to color in this figure legend, the reader is referred to the web version of this article.)

Electron microprobe traverses were conducted across the margins of select inclusions to document chemical zoning profiles in melilite. Wavelength-dispersive (WDS) analyses were obtained with a Cameca SX-50 electron microprobe operated at 15 kV at The University of Chicago. The WDS data were reduced using the modified ZAF correction procedure PAP (Pouchou and Pichoir, 1984). For Efremovka sample Ef-1, melilite compositions were obtained using the SX-100 electron microprobe at JSC. The JSC electron probe was operated at 15 kV with a 20 nA beam current, and also used PAP data reduction.

2.3. Modeling oxygen isotopic exchange in CAIs

Assuming that the gradients defined by O-isotopic profiles in the interiors of CAIs were established by incomplete exchange between a primordial, or other initial, isotopic composition characteristic of the CAI interior and an external isotopic reservoir, oxygen diffusion models were used to assess the timescale for establishing the observed profiles. For non-steady state diffusion in spherical coordinates, Eq. 6.18 of Crank (1975),

$$\frac{C - C_{i,cond}}{C_0 - C_{i,cond}} = 1 + \frac{2a}{\pi r}\sum_{n=1}^{\infty}\frac{(-1)^n}{n} sin\frac{n\pi r}{a} exp(-D_i n^2 \pi^2 t/a^2) \quad (1)$$

was used to determine $(C–C_{i,cond})/(C_0–C_{i,cond})$ as a function of r, the distance from the edge of the inclusion of radius a; and t, time; where $C_{i,cond}$ is an initially uniform concentration of a particular oxygen isotope in the condensed phase, assumed to be melilite, either crystalline or its molten equivalent; C_0 is the surface concentration of the same isotope, assumed to be constant; C is the concentration of that isotope at r and t; and D_i is the temperature-dependent diffusivity of each isotope in the solid-state from Ryerson and McKeegan (1994) and in Type A and B melts using the viscosity-based parameterization of Liang et al. (1996), respectively. Computed profiles for each isotope were combined to obtain profiles for $\Delta^{17}O$. $C_{i,cond}$ was inferred from $\Delta^{17}O$ analyses of either interior spinel or uniform melilite. Various isotopic compositions were used for C_0: either $\Delta^{17}O$ of the innermost WL rim layer; the Allende matrix composition for testing parent body exchange scenarios; or an assumed planetary-like oxygen isotopic composition of an ambient solar nebular gas. For nebular exchange models, the sum of the partial pressures of all oxygen-containing gas species, $\sim 10^{-6}$ bar, obtained from solar gas equilibrium condensation calculations at 1400 K and $P^{tot} = 10^{-2}$ or 10^{-3} bar (Fedkin and Grossman, 2006), was used to obtain C_0. For parent body scenarios, the abundance of oxygen at the inclusion surface reflects that of an Allende matrix composition (Clarke et al., 1970). Diffusion times were calculated at 1400 K and 900 K for nebular and parent body exchange, respectively.

3. RESULTS

3.1. Petrography of refractory inclusions

The petrography of the CAIs included in this study has been described in detail elsewhere (Meeker et al., 1983; Simon et al., 1999, 2001; Simon and Grossman, 2013). The CAIs are igneous with a range of mineral assemblages: the compact Type A CAIs are dominated by blocky, coarse-grained melilite and fassaite enclosing euhedral spinel grains and anhedral perovskite grains; the Type B CAIs have more abundant fassaite than the Type A CAIs, with coarse-grained anorthite and melilite enclosing smaller spinel grains. Like most CAIs, those studied here likely experienced one or more reheating events that led to such processes as melting, solid-state recrystallization, and possibly reactions between primary phases and an external reservoir (e.g., MacPherson and Davis, 1993; Hsu et al., 2000; Simon and Young, 2011). Varying abundances of

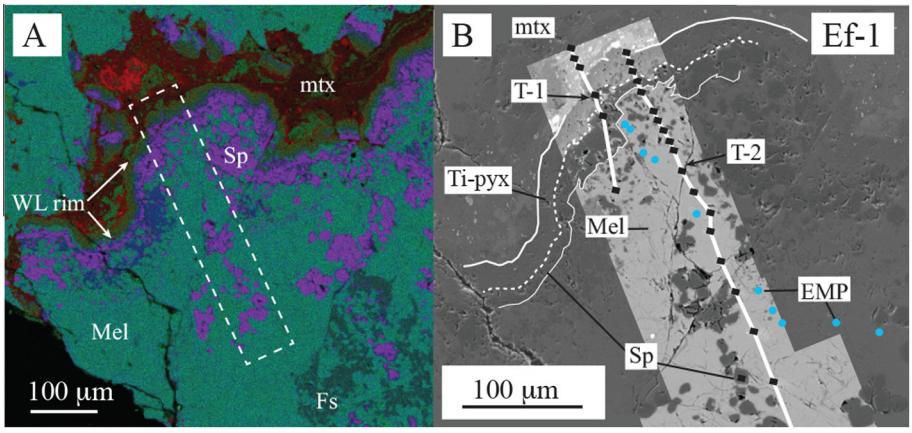

Fig. 2. Images of compact Type A inclusion Ef-1. (A) Low-magnification, false-color X-ray map (Mg = red, Ca = green, Al = blue), showing occurrence of spinel (purple), pyroxene (dark green and olive green), and melilite (blue-green) in the interior of the inclusion and the WL rim. Olivine is red and epoxy is black. Region of interest indicated by the white dashed-line rectangle. (B) Backscattered electron image overlain upon a secondary electron image, showing the locations of NanoSIMS traverses (T-1, T-2; black rectangles) and electron microprobe transect (EMP; blue circles) in the WL rim and margin. Some measurements are located further toward the center of the inclusion, beyond the field of view. Mel: melilite; Sp: spinel; Ti-pyx: Ti-bearing pyroxene; mtx: matrix. Size of analysis spots enhanced by 2× for clarity. (For interpretation of the references to color in this figure legend, the reader is referred to the web version of this article.)

secondary minerals are found in the inclusions, consistent with differences seen previously in CAIs from oxidized and reduced chondrites (Brearley and Jones, 1998, and references therein). The suite of inclusions studied here represents a range in the degree of secondary alteration, from least to most: Ef-1/L6, A37, Egg-6, TS4, and ALH3. Images of the samples are shown in Figs. 2–7.

3.1.1. Compact Type A CAIs: Ef-1 (Efremovka), L6 (Leoville), ALH3 (Allende), and A37 (Allende)

Ef-1 (Efremovka), Fig. 2, is a convoluted compact Type A CAI, ~3 × 3.5 mm, composed mainly of visually unaltered melilite and 20–70 μm-sized spinel grains, with interstitial, anhedral fassaite. The inclusion is surrounded by a simple ~15–40 μm thick WL rim made up, from the interior outwards, of spinel and pyroxene (Fig. 2A and B). Melilite in Ef-1 is largely gehlenitic ($Åk_{10\pm2}$), except at the outermost edge where it is slightly more magnesian (~$Åk_{17}$), as shown in Fig. 8A. Representative melilite analyses are given in Table 2.

L6 (Leoville), Fig. 3, is a visually unaltered compact Type A inclusion, originally ~6–7 mm, with clusters of spinel grains (typically euhedral, ~50 μm across) and fassaite (anhedral) enclosed in melilite. At the edge of L6, a nearly continuous, thick (up to 100 μm) WL rim layer consists of spinel intergrown with melilite. Outside the main spinel layer, there are additional occurrences of pyroxene ± melilite layers. Based on petrography and mineral chemistry, five generations of pyroxene (Fig. 3B–D) were identified (Simon and Grossman, 2013) outside of the innermost spinel layer. Representative electron probe analyses of each of these five generations are given in Table 3. The innermost pyroxene layer (Ti-pyx-1) is Ti-rich and intergrown with the "main" spinel layer. This pyroxene layer (⩽10 μm thick) has a sharp contact with a zoned pyroxene layer (Ti-pyx-2) that becomes less Ti-rich outward and is in contact with a layer of varying thickness consisting of melilite and spinel.

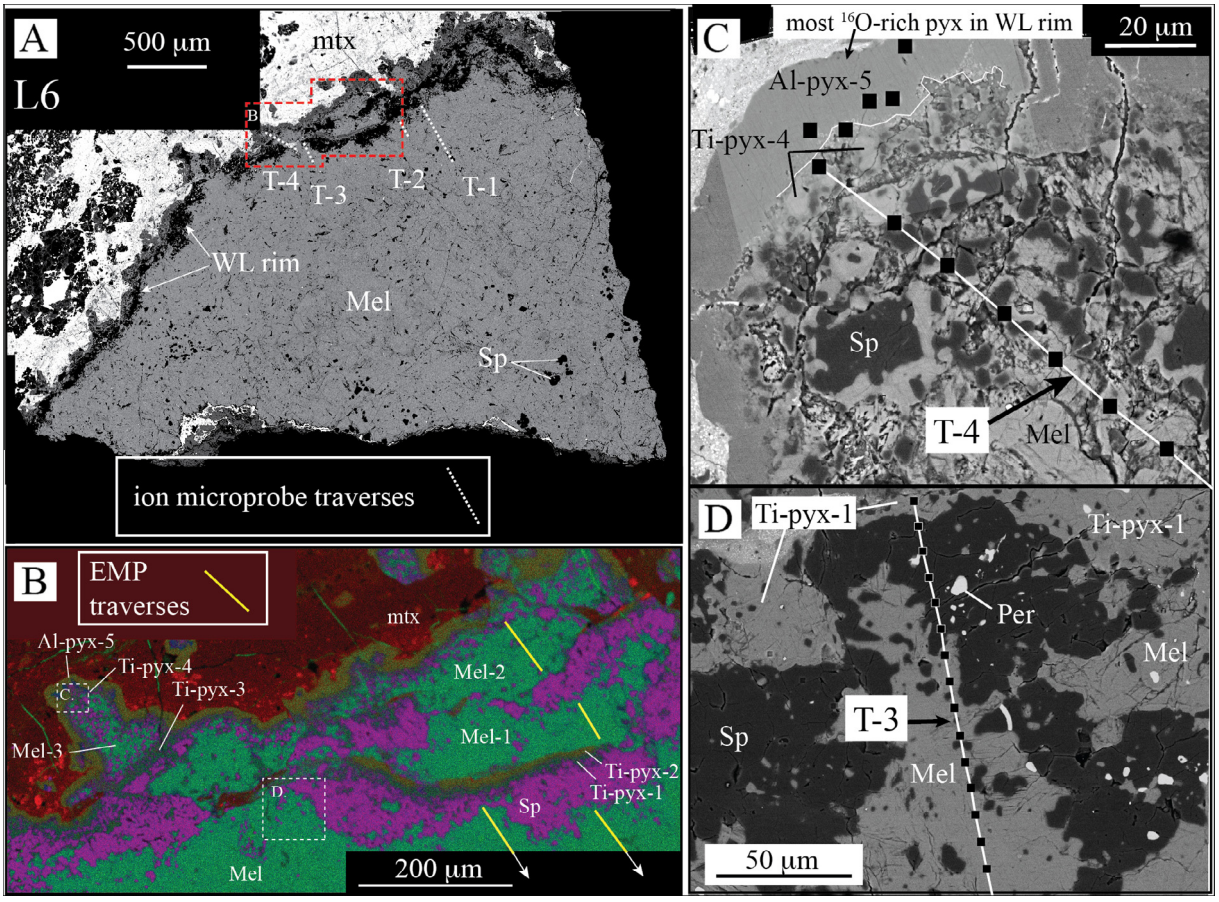

Fig. 3. Images of compact Type A inclusion L6. (A) Backscattered electron image of section, showing sparse spinel in the melilite-rich interior, spinel-rich WL rim, and meteorite matrix. Locations of NanoSIMS traverses (T-1 to T-4) and the area shown in B. (red dashed-line region) are indicated. Epoxy is black. (B) False-color X-ray map (Mg = red, Ca = green, Al = blue), showing occurrence of spinel (purple) and pyroxene (dark green and olive green) and melilite (blue-green) at the rim and olivine (red) in the matrix. Locations of electron microprobe analytical traverses (yellow lines) and areas shown in C and D (white dashed-line rectangles) are indicated. (C) Backscattered electron image of the location of Traverse 4 (T-4), which sampled the outer granular melilite and spinel unit Mel-3 and pyroxene units Ti-pyx-4 and Al-pyx-5, the latter being the outermost, continuous diopside layer. (D) Backscattered electron image of the location of Traverse 3 (T-3), which sampled melilite, spinel, and pyroxene unit Ti-pyx-1 (black rectangles). Abbreviations as used previously, plus Per: perovskite. Size of NanoSIMS analysis spots enhanced by 50% for clarity. (For interpretation of the references to color in this figure legend, the reader is referred to the web version of this article.)

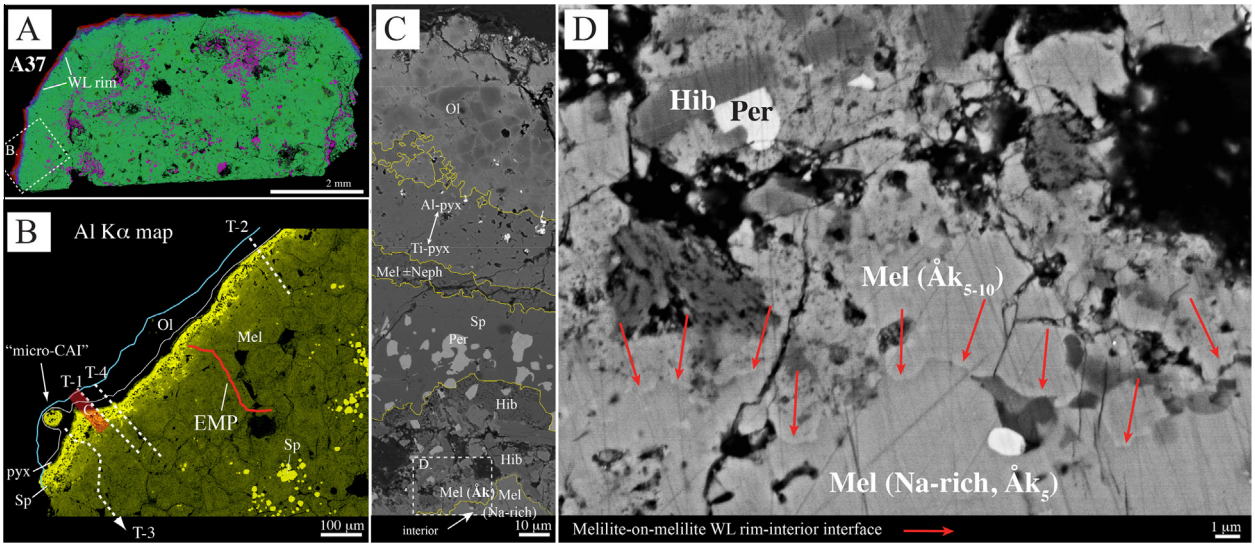

Fig. 4. Images of compact Type A inclusion A37. (A) False colored X-ray map (Mg = red, Ca = green, Al = blue) of entire section, showing varying concentrations of spinel in the melilite-rich interior. WL rim section and area shown in B. are indicated. (B) Aluminum (Al Kα) X-ray map of region with NanoSIMS traverses (T1 to T4) and electron microprobe (EMP) transects of Simon et al. (2011) are indicated. Melilite composition zoning (increasing Al content) at the edge of the inclusion and within individual melilite grains can be discerned. Area shown in C is indicated by red-shaded rectangle. (C) Backscattered electron image of WL rim layers from inside out include melilite (Mel Åk); hibonite (Hib) ± perovskite (Per); melilite (Mel) ± nepheline (Neph); pyroxene (pyx) zoned from Ti-rich to Al-rich; and olivine (Ol). Area shown in D is indicated by dashed-line rectangle at bottom. (D) Backscattered electron image of melilite-on-melilite WL rim-interior interface, indicated by red arrows. (For interpretation of the references to color in this figure legend, the reader is referred to the web version of this article.)

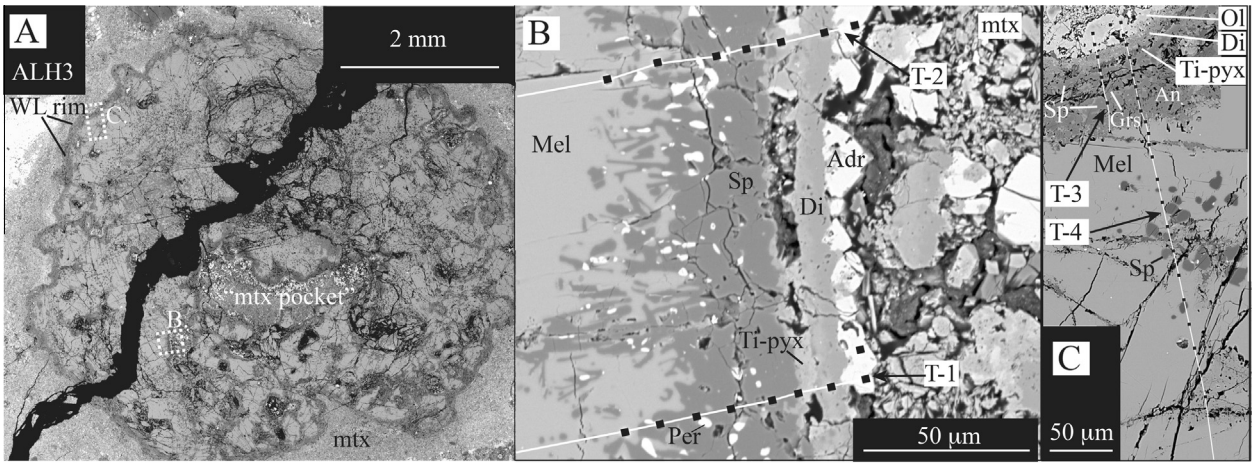

Fig. 5. Backscattered electron images of Type A inclusion ALH3. (A) View of entire section showing WL rim and locations (white dashed-line rectangles) of areas shown in B and C. (B) Locations of NanoSIMS traverses 1 and 2 (T-1 and T-2). (C) Locations of NanoSIMS traverses 3 and 4 (T-3 and T-4). Abbreviations as used previously, plus Adr: andradite; Grs: grossular. Size of NanoSIMS analysis spots enhanced by 50% for clarity.

Two other Ti-rich pyroxene units (Ti-pyx-3; Ti-pyx-4) with distinct compositions occur (Simon and Grossman, 2013). Finally, the entire inclusion and inner rims are surrounded by a uniform layer of diopside (~15 μm, Al-pyx-5, Fig. 3C), that in some places is in direct contact with the Ti-bearing pyroxene of an inner layer but more commonly overlies the irregular, granular mixed melilite-spinel layer.

In L6 melilite is found in several rim layers that range in grain size and, in places, are locally bifurcated by discontinuous spinel layers (Fig. 3B). The åkermanite content in the innermost layer (Mel-1) decreases radially outward from ~$Åk_{15}$ to ~$Åk_5$. The åkermanite content in the next layer (Mel-2) increases radially outward from ~$Åk_5$ to ~$Åk_{13}$ (see Fig. 8B). In places, the innermost melilite can be found in contact with the "main" spinel layer rather than the inner Ti-rich zoned pyroxene layer (Ti-pyx-2). The third occurrence of rim melilite (Mel-3) is found in "peninsulas" sitting on top of pyroxene layer Ti-pyx-3. It has a range of grain

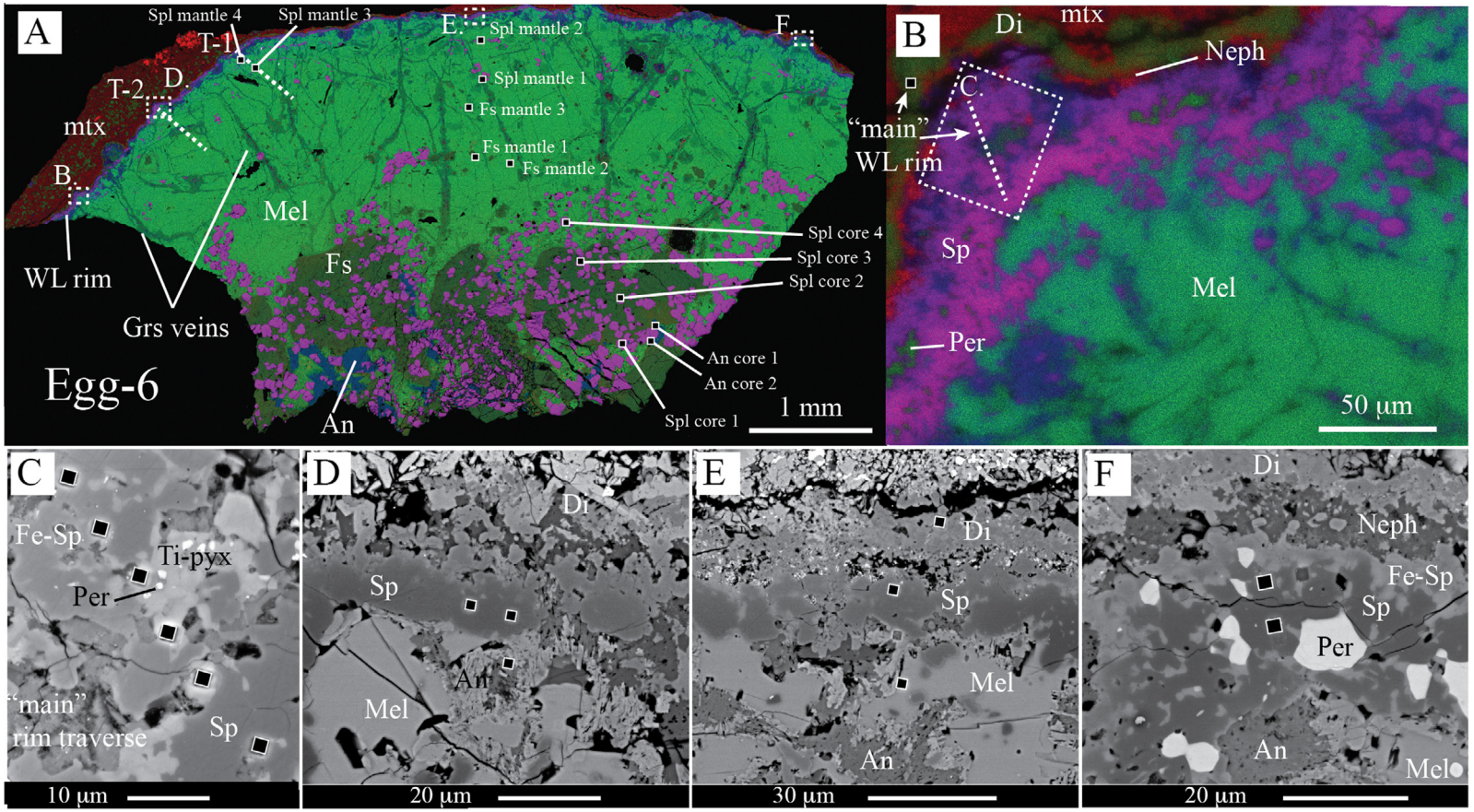

Fig. 6. Images of Type B1 inclusion Egg-6. (A) Low-magnification, false-color X-ray map (Mg = red, Ca = green, Al = blue) of entire section, showing spinel (purple), fassaite (coarse, dark green grains), melilite (light green) and anorthite (blue) in the interior of the inclusion, and grossular veins (dark green) across the mantle. Olivine is red and epoxy is black. Interior NanoSIMS analysis locations are indicated by black rectangles and traverses, T-1 and T-2 (white dashed-lines). Areas shown in B–F are indicated by dashed-line rectangles where the main WL rim traverse and additional WL rim analyses were made. (B) False-color X-ray map of rim region that includes the area shown in C (colors and phases as in A). (C) Backscattered electron image (BEI) of the location of the main WL rim NanoSIMS traverse that sampled spinel and Ti-pyroxene rim layers. (D) BEI of locations of NanoSIMS analyses measured at the end of T-2. (E) BEI showing locations of NanoSIMS spots in melilite, spinel and diopside in the WL rim. (F) BEI showing locations of NanoSIMS spots in spinel. Abbreviations as used previously. Size of NanoSIMS analysis spots enhanced by 50% for clarity. (For interpretation of the references to color in this figure legend, the reader is referred to the web version of this article.)

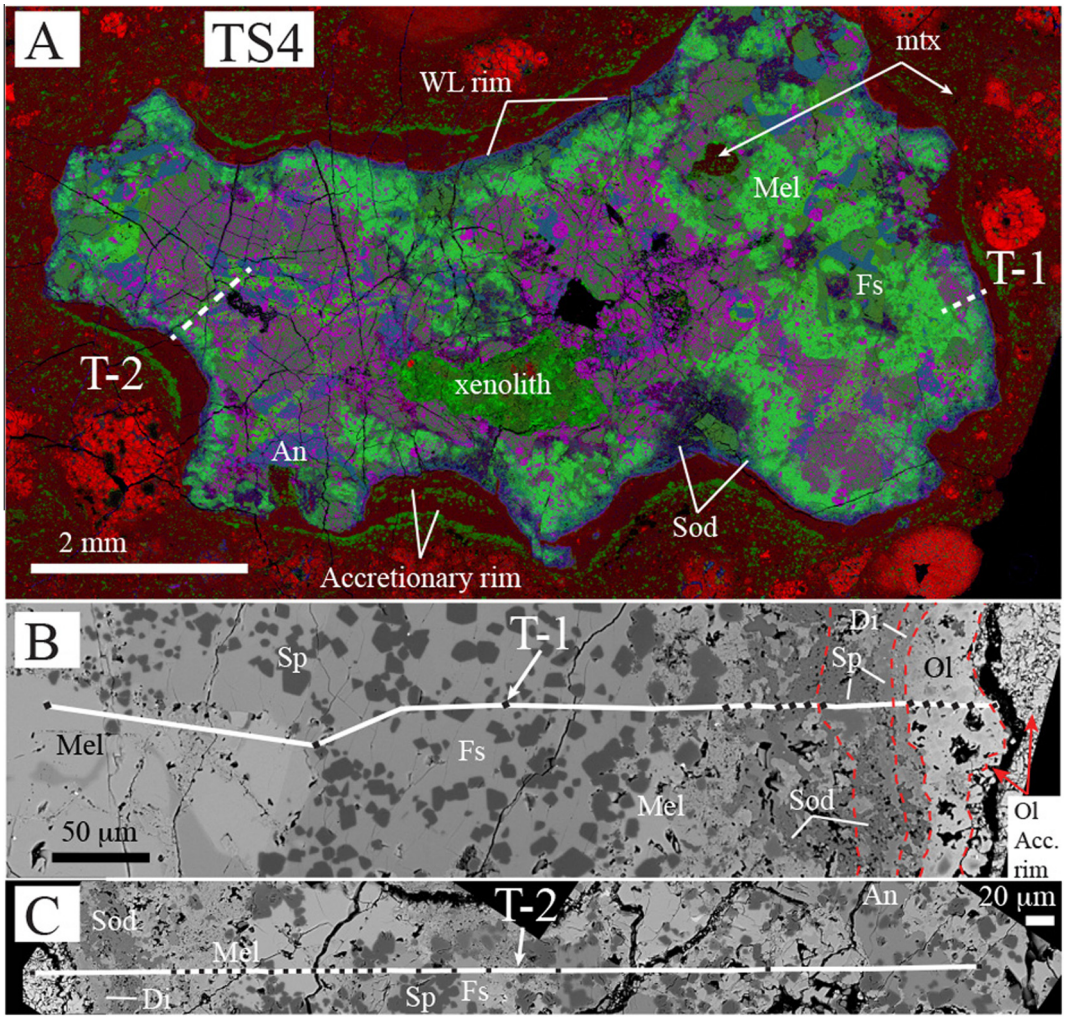

Fig. 7. Images of Type B2 inclusion TS4. (A) Low-magnification, false-color X-ray map (Mg = red, Ca = green, Al = blue) of entire section, showing spinel (purple), fassaite (dark green), melilite (light green) and anorthite (blue). Olivine is red, epoxy is black, and secondary pyroxene within, but mostly defining the outer edge of the accretionary rim, is forest green. Two NanoSIMS traverses, T-1 and T-2, are indicated by the white dashed-lines. (B) BEI showing the NanoSIMS Traverse 1, from the interior (left) to the rim (right) of the inclusion. Individual rim layers are outlined in red dashed-lines. (C) BEI showing the NanoSIMS Traverse 2, from the interior (right) to the rim (left) of the inclusion. Abbreviations as used previously, plus Sod: sodalite. Size of NanoSIMS analysis spots enhanced by 50% for clarity. (For interpretation of the references to color in this figure legend, the reader is referred to the web version of this article.)

sizes that appear to correlate with spinel content, with the coarser melilite enclosing fewer spinel grains. Across the outer ~200 µm of the inclusion, the åkermanite content of the melilite decreases radially outward, from $Åk_{30}$ to $Åk_3$.

Based on electron microprobe analyses summarized in Table 3, all of the WL rim pyroxene layers surrounding L6 exhibit lower Ti^{3+}/Ti^{tot} than those measured in the interior fassaite (0.71) similar to that reported elsewhere for other WL rims, e.g., Dyl et al. (2011). In detail, Ti^{3+}/Ti^{tot} decreases from the innermost layer, Ti-pyx-1 (0.57), to Ti-pyx-2 (0.42, inner sublayer), to Ti-pyx-2 (~0, outer sublayer). Then there is a reversal toward slightly higher Ti^{3+}/Ti^{tot} in Ti-pyx-3 (0.29) and Ti-pyx-4 (0.46). Scarce titanium is measured in the outermost diopside layer (Table 3). There is a range of Ti^{3+}/Ti^{tot} in each layer when individual analyses are considered, showing greater overlap between the layers. These pyroxene layers provide an opportunity for the first coordinated report of O-isotopes and oxidation state.

A37 (Allende), Fig. 4, is a subspherical, compact Type A inclusion, ~4x7 mm, composed primarily of melilite ($Åk_{5–36}$), 20–70 µm-sized spinel grains and rare fassaite mainly occurring between the melilite grains (Simon et al., 2011 and references therein). The melilite near the outer margin of the inclusion is zoned in composition from Mg-rich toward the interior to Al-rich toward the edge (Fig. 8C). The surrounding WL rim is ~50 to 100 µm thick and made up of a typical layered mineral sequence, from the interior outward, of hibonite ± melilite, spinel (enclosing perovskite), melilite/nepheline, Ti-bearing pyroxene, Al-rich pyroxene and an outermost layer of olivine (Fig. 4B). A small (~50 µm diameter), spinel-rich, perovskite-bearing "micro-CAI" is located within the WL rim layers (Simon

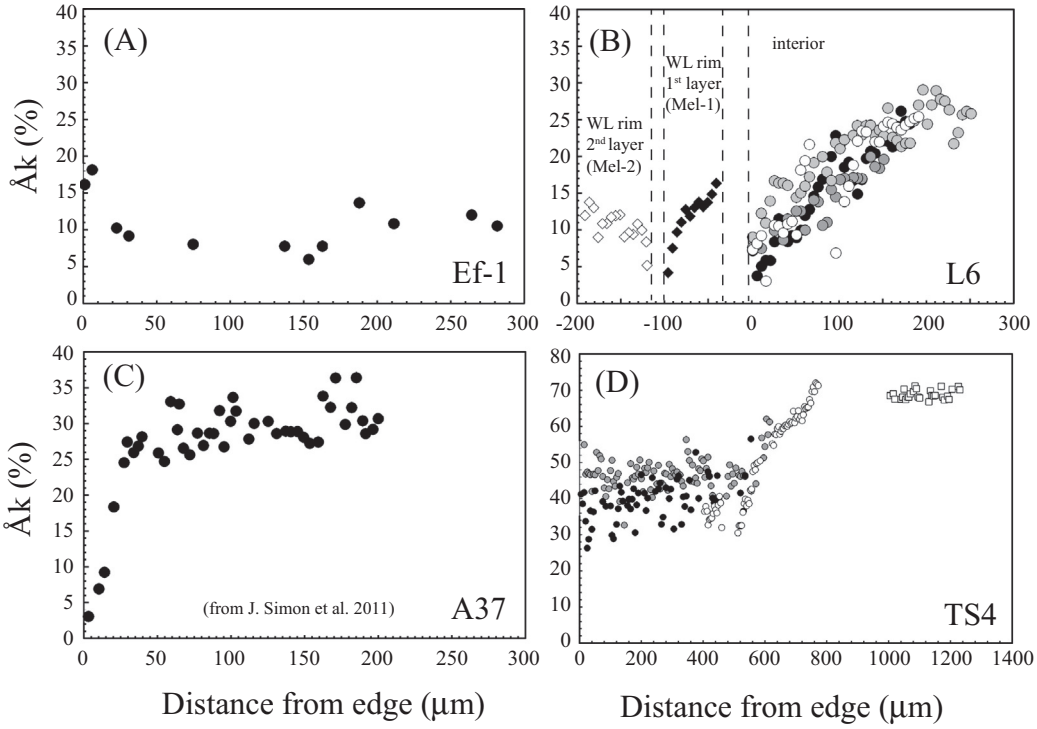

Fig. 8. Melilite compositions (mole% åkermanite), determined by electron microprobe, as a function of distance from the edge of the inclusion interior (i.e., the contact between the inclusion and WL rim) in four of the inclusions in the present study. (A) Compact Type A inclusion Ef-1. A slight increase in Åk content is seen at the rim. (B) Compact Type A inclusion L6. This sample has multiple rim units, as indicated; distances are measured from the innermost rim inward (positive values) or outward (negative values). Circles and diamonds represent analyses of interior and rim melilite, respectively. The different symbol shades represent different EMP traverses. (C) Compact Type A inclusion A37. Data from Simon et al. (2011). (D) Type B2 inclusion TS4. Squares represent analyses of interior melilite, circles are data from traverses across the margin. The different symbol shades represent different EMP traverses.

Table 2
Representative electron probe analyses of melilite.

	1	2	3	4	5	6	7	8	9	10
Na_2O	0.03	0.02	0.04	0.02	0.02	0.00	0.02	0.02	0.18	0.13
MgO	2.61	1.18	1.61	1.49	1.84	2.10	0.87	4.14	6.90	4.62
Al_2O_3	31.80	33.62	32.38	33.13	31.21	30.40	33.76	25.33	18.67	23.68
SiO_2	25.42	24.20	24.87	23.49	24.55	24.78	22.35	27.37	33.26	28.94
CaO	39.78	40.13	40.17	40.27	40.93	41.04	41.02	40.89	40.91	40.69
TiO_2	0.07	0.02	0.09	0.00	0.01	0.04	0.08	0.00	0.02	0.04
Cr_2O_3	0.02	0.00	0.01	n.d.	n.d.	n.d.	n.d.	n.d.	n.d.	n.d.
MnO	0.01	0.02	0.01	n.d.	n.d.	n.d.	n.d.	n.d.	n.d.	n.d.
FeO	0.14	0.08	0.01	0.13	0.01	0.05	0.00	0.00	n.d.	n.d.
SUM	99.91	99.28	99.19	98.54	98.56	98.41	98.10	97.76	99.94	98.10
Cations per 7 oxygens										
Na	0.003	0.002	0.004	0.002	0.002	0.000	0.002	0.002	0.016	0.012
Mg	0.177	0.081	0.110	0.103	0.127	0.146	0.061	0.289	0.468	0.321
Al	1.705	1.816	1.750	1.809	1.706	1.666	1.860	1.397	1.001	1.299
Si	1.157	1.109	1.141	1.089	1.139	1.153	1.045	1.281	1.513	1.347
Ca	1.939	1.971	1.974	2.000	2.034	2.045	2.054	2.051	1.994	2.029
Ti	0.002	0.000	0.003	0.000	0.000	0.001	0.003	0.000	0.001	0.002
Fe	0.005	0.003	0.000	0.005	0.000	0.002	0.000	0.000	–	–
Total	4.989	4.983	4.983	5.008	5.009	5.013	5.024	5.021	4.993	5.008
Åk	17.2	8.2	11.1	9.2	14.3	16.0	5.7	29.1	50.6	34.9

1: Ef-1, edge. 2, 3: Ef-1, interior. 4–6: L6, outer melilite. 7, 8: L6, inner melilite. 9, 10: TS4. n.d.: not determined.

Table 3
Electron probe analyses of pyroxene in L6.

	1	2	3	4	5	6	7
MgO	6.98	5.37	13.47	17.77	7.34	4.66	18.98
Al_2O_3	19.33	23.51	9.94	3.42	24.06	25.59	1.00
SiO_2	33.12	29.54	43.38	51.54	30.47	27.79	52.10
CaO	24.49	24.73	24.63	24.99	23.92	24.74	24.86
Ti as TiO_2	14.30	15.70	7.38	2.38	11.92	15.97	0.13
Sc_2O_3	0.21	BDL	BDL	BDL	0.06	0.14	BDL
V_2O_3	0.58	0.62	0.09	BDL	0.61	0.93	0.02
FeO	0.02	0.02	0.00	BDL	0.37	0.18	0.74
Ti_2O_3	9.18	8.13	2.74	—	3.04	7.47	—
TiO_2	4.22	6.88	4.27	—	8.35	7.86	—
Sum	98.30	98.80	98.51	100.10	98.15	99.20	98.26
Si	1.275	1.142	1.610	1.868	1.149	1.071	1.933
Al	0.725	0.858	0.390	0.132	0.851	0.929	0.044
Al	0.155	0.214	0.044	0.014	0.218	0.233	0.000
Mg	0.400	0.310	0.745	0.959	0.413	0.268	1.049
Fe	0.001	0.001	0.000	0.000	0.012	0.006	0.023
Sc	0.007	0.000	0.000	0.000	0.002	0.005	0.000
V	0.017	0.018	0.003	0.000	0.017	0.027	0.001
Ti^{3+}	0.295	0.259	0.086	–	0.097	0.238	–
Ti^{4+}	0.122	0.198	0.120	0.065	0.241	0.225	0.004
Ca	1.000	1.000	1.000	0.951	1.000	1.000	0.988
Ti^{3+}/Ti^{tot}	0.707	0.567	0.417		0.287	0.463	

1. Interior, coarse fassaite, average of 25 analyses. 2. Ti-pyx-1 layer. 3. Ti-pyx-2 (inner zone) 4. Ti-pyx-2 (outer zone). 5. Ti-pyx-3. 6. Ti-pyx-4 7. Al-pyx-5 outermost (diopside) rim. For Ti-rich analyses, Ti^{3+}/Ti^{4+} proportions calculated according to the method of Simon et al. (1991), with normalization of analyses to one Ca and four total cations per six oxygen anions. BDL: Below detection limit of electron microprobe of 0.02 wt%.

et al., 2011). Melilite contained in the hibonite ± melilite rim layer is locally in contact with melilite of the host inclusion (Fig. 4C).

ALH3 (Allende), Fig. 5, is a large, subspherical Type A inclusion, ~6 mm, consisting of melilite, hibonite, and spinel (Simon et al., 2001). The range of melilite compositions is similar to that of other Type A inclusions ($Åk_{1–29}$), but there is neither an inclusion-wide trend nor a dominant core-rim trend within individual crystals (Simon et al., 2001). Surrounding the CAI is an ~30–75 μm thick rim containing: (1) secondary anorthitic plagioclase; (2) spinel; (3) Ti-pyroxene; (4) nepheline (discontinuous layer); (5) Al-diopside; and (6) Fe-rich olivine, $\sim Fa_{50}$, which may be accretionary (Fig. 5B). The inclusion encloses a pocket of matrix, with a second, 'interior' WL rim sequence lining the pocket, varying from ~50 to 100 μm in thickness and consisting of: (1) secondary anorthitic plagioclase (a discontinuous layer of varying thickness); (2) spinel (enclosing perovskite); (3) Ti-bearing pyroxene; (4) Al-diopside; and (5) andradite (Fig. 5C). The primary difference between the sequences is the outermost layer, i.e., Fe-rich olivine versus andradite.

3.1.2. Type B CAIs: Egg-6 (Allende) and TS4 (Allende)

Egg-6 (Allende), Fig. 6, is a subspherical Type B1 inclusion, ~2 cm, with a core of fassaite, anorthite, spinel, and melilite surrounded by a well-developed melilite ($Åk_{20–60}$) mantle zoned from Mg-rich toward the interior to Al-rich toward the edge. One quarter of the inclusion is composed of secondary minerals that are typical of those found in alteration veins in Allende CAIs (MacPherson et al., 1981; Meeker et al., 1983), but this high degree of alteration was not seen in the section, ~3 × 6 mm, used for this study. The outer ~20–40 μm of the sample consists of a simple WL rim of Fe-poor spinel that has a slight increase in FeO grading outward, which is surrounded by a layer of diopside (Fig. 6B and D–F). The spinel layer encloses a semi-continuous chain of isolated perovskite and Ti-bearing pyroxene grains (Fig. 6B, C, and F).

TS4 (Allende), Fig. 7, is an irregularly-shaped Type B2 CAI, ~5 × 8 mm, composed mainly of melilite ($Åk_{35–50}$), fassaite, anorthite, and 5–70 μm-sized spinel grains found throughout and in palisades. The interior is rich in fassaite and anorthite that typically poikilitically encloses high concentrations of spinel grains (Fig. 7A and B). TS4 is surrounded by an ~15–60 μm thick WL rim composed, from the interior outward, of spinel, Ti-bearing pyroxene, Al-rich pyroxene, and an outermost band of olivine (Fig. 7B and C). Outward from the WL rim is a fine-grained olivine accretionary rim. The margin of the inclusion is locally melilite-rich, with grains that zone from Mg-rich toward the interior to Al-rich toward the edge of the inclusion (Fig. 8D). Secondary minerals include patchy nepheline and sodalite at the edge of the CAI and andradite + wollastonite + hedenbergite in what appears to be a discrete pod or xenolith in the interior.

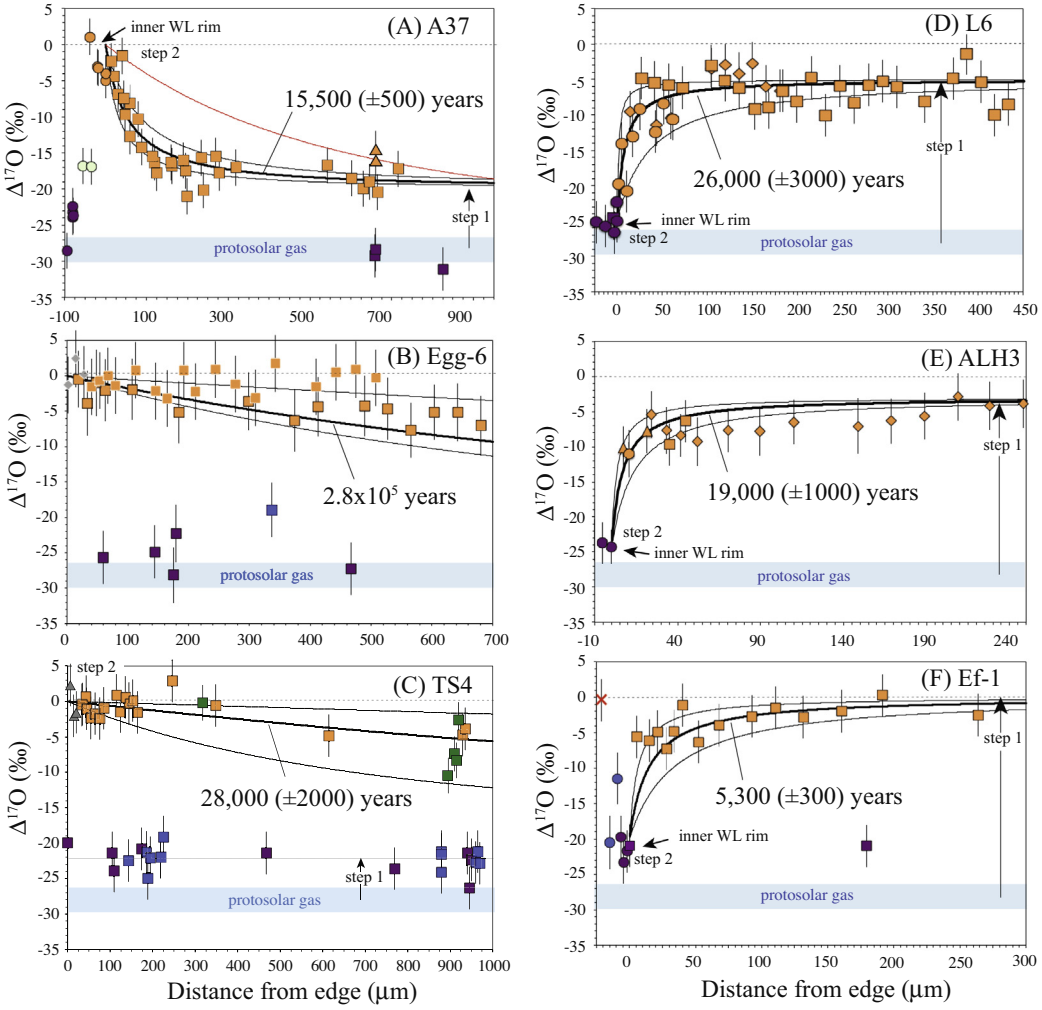

Fig. 9. Oxygen isotopic zoning profiles across the margins of (A) Allende A37, (B) Allende Egg-6, (C), Allende TS4, (D) Leoville L6, (E) Allende ALH3, and (F) Efremovka Ef-1. Primary minerals are color-coded: melilite-tan, spinel-purple, fassaite-blue, perovskite-light green, anorthite-dark green and olivine-red. For the primary phases different symbol shapes or borders indicate different traverses. All secondary minerals are gray: plagioclase (triangles), and sodalite (diamonds). Also shown are modeled diffusion profiles, discussed in text and summarized in Table 4. For consistency, all models shown reflect calculations for diffusive exchange of oxygen at 1400 K between interior solid melilite and a nebular gas reservoir, assumed to have $P^{tot} = 10^{-3}$ bar. Blue band labeled "protosolar gas" is the solar gas composition of McKeegan et al. (2011). The red curve in (A) is representative of the mismatch of single-step models for A37. The black curves in (A) reflect the cumulative effects of two-steps of oxygen exchange, the first that reset melilite to an intermediate $\Delta^{17}O$ value (step 1), implied by the relatively uniform value measured in the interior, before melilite at its margin exchanged further with a near-zero $\Delta^{17}O$ planetary reservoir (step 2). In (B) single-step models (black curves) can be matched to the data, assuming the inclusion initially had a protosolar $\Delta^{17}O$ composition and then experienced oxygen exchange that transformed its $\Delta^{17}O$ to those of the interior melilite. In (C), interior spinel and fassaite have similar $\Delta^{17}O$ values of -22 ± 2‰, whereas melilite is relatively ^{16}O-poor and exhibits constant to slightly increasing $\Delta^{17}O$ toward the edge of the inclusion. Model curves reflect two-steps of exchange, where first the inclusion equilibrates with a reservoir of intermediate $\Delta^{17}O$ composition, recorded by the similarity of its spinel and fassaite (step 1), before melilite exchanged further as in (A) (step 2). For (D, E, and F), the reversely zoned CAIs, the model curves were calculated as above, except that the interior melilite values were used for the initial CAI value and the nebular gas reservoir was assumed to have the same $\Delta^{17}O$ as the spinel in the WL rims (see Table 4). (For interpretation of the references to color in this figure legend, the reader is referred to the web version of this article.)

3.2. NanoSIMS oxygen isotope measurements

3.2.1. Isotopic zoning profiles across the margins of inclusions

Oxygen isotopic results that have been corrected for mineral-specific IMF effects are presented in Figs. 9 and 10. Both mineral-specific and average IMF corrected data are listed in Table 1. Also shown in these figures are modeled diffusion profiles, discussed in later sections and summarized in Table 4. In the following paragraphs, we describe the profiles as either "normal", i.e. profiles that exhibit ^{16}O-enrichments that decrease with distance from the center of the inclusion, or "reverse". The A37 and L6 profiles are the most distinctive examples of normal and reverse profiles, respectively. The two Type B CAIs, Egg-6 and TS4, are most consistent with normal zoning profiles, whereas Ef-1 and ALH3 are more consistent with reverse

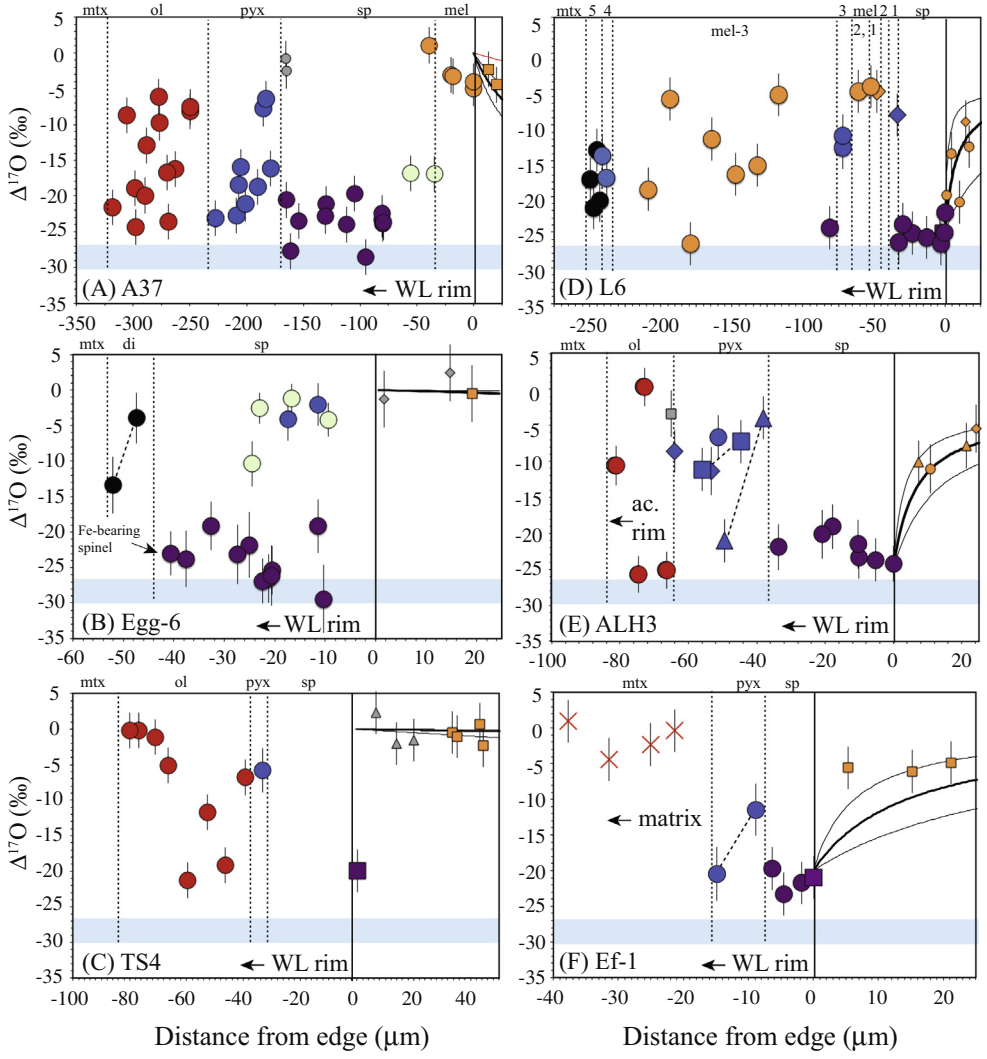

Fig. 10. Oxygen isotopic variability among Wark–Lovering rim layers surrounding (A) Allende A37, (B) Allende Egg-6, (C) Allende TS4, (D) Leoville L6, (E) Allende ALH3, and (F) Efremovka Ef-1. Solid and dashed vertical lines indicate contacts between rims and interiors, and between individual WL rim layers, respectively. Layers are further identified by phase labels along the tops of the plots. Numbers in (D) are L6 pyroxene layer units. Diagonal dashed lines connect pyroxene analyses that exhibit "reverse" isotopic zoning within a single analytical transect. Color-coding and solid curves as in Fig. 9, plus diopside (black circles), accretionary olivine (red X's), secondary nepheline (gray circles in (A)) and andradite (gray square in (E)). (For interpretation of the references to color in this figure legend, the reader is referred to the web version of this article.)

zoning profiles. The contact between melilite at the outer edge of an inclusion (i.e., the margin) and its WL rim is a feature common to all of the studied inclusions. Therefore, analysis points within the WL rim and the inclusion interior are plotted as a function of negative and positive distance from this contact, respectively, in Figs. 9 and 10. Unless stated otherwise, the uncertainties for all of the individual $\Delta^{17}O$ values are ~4‰ (2 se). In order to assess whether specific regions or rim layers have different oxygen isotopic compositions, the averages of multiple measurements within these materials are compared. In some instances only a few measurements define the average value. To account for the statistics of small numbers, 95% confidence intervals are determined by multiplying the standard errors (se) by a Student's *t*-adjustment (Mahon, 1996).

3.2.1.1. A37. The $\Delta^{17}O$ of melilite within the outer 100 μm of A37 increases monotonically outward from -17.5 ± 0.8‰ ($n = 20$), characteristic of the interior, to -2.2 ± 3.0‰ ($n = 6$) at the edge (Fig. 9A). Additional melilite analyses reported here match the composition of the interior melilite ($\Delta^{17}O \sim -18$‰) reported by Simon et al. (2011), and replicate analyses of interior spinel grains had reproducible, relatively ^{16}O enriched $\Delta^{17}O$ values ranging from −28‰ to −31‰ ($n = 3$).

3.2.1.2. Egg-6. Two traverses across the melilite mantle (Fig. 9B) were complemented by analyses of fassaite, spinel, and anorthite in the margin and/or within the core of this Type B1 inclusion. Melilite measurements yield an average $\Delta^{17}O$ value of -2.3 ± 0.9‰ ($n = 32$, squares). Melilite

Table 4
Summary of diffusion exchange models.

Inclusion	Size (cm)[*]	Early stage ("Step 1")		Environments		Later stage ("Step 2")		Environments	
		$\Delta^{17}O$ (‰) Interior	$\Delta^{17}O$ (‰) Gas	Nebular T (K), t (years)	Parent body T (K), t (years)	$\Delta^{17}O$ (‰) Interior	$\Delta^{17}O$ (‰) Gas	Nebular T (K), t (years)	Parent body T (K), t (years)
Idealized CAIs									
Molten	0.5	−28	0	1773, 10^0	Nil				
Molten	0.5	−28	0	1973, $\leqslant 10^{-3}$	Nil				
Solid	0.5	−28	0	1400, 2.5×10^4	Nil				
Solid, $P_{tot} = 10^{-2}$	0.5	−28	0	1500, 2×10^3	Nil				
Defects[RM]	2.0	−28	0	1400, 10^3	900, $\geqslant 10^6$				
Defects[RM]	0.5	−28	0	1500, 10^2	900, 10^6				
Studied CAIs									
A37	0.5	−28	−20	1400, $\leqslant 2 \times 10^4$[m]	1000, $\geqslant 10^8$	−20	0	1400, $\leqslant 1.6 \times 10^4$	900, $\geqslant 10^8$
Egg-6	2.0	−28	0[t]	1400, $\leqslant 2.8 \times 10^5$	900, 10^9[**]				
TS4	0.6	−28	−20	1400, $\leqslant 2 \times 10^4$[m]	1000, 10^8	−20	0[t]	1400, $\leqslant 3 \times 10^4$	900, $\geqslant 10^8$
ALH3	0.6	−28	0	1400, $\leqslant 2.5 \times 10^4$[m]	1000, 10^8	−3	−25	1400, $\leqslant 2 \times 10^4$	900, $\geqslant 10^8$
Ef-1	0.3[f]	−28	0	1400, $\leqslant 10^3$[m]	900, $\geqslant 10^8$[**]	0	−20	1400, $\leqslant 5 \times 10^3$	–
L6	0.7[f]	−28	0	1400, $\leqslant 3 \times 10^4$[m]	900, $\geqslant 10^8$[**]	−5	−25	1400, $\leqslant 3 \times 10^4$	–

[*] Spherical diameter used for model calculations.
[f] Original inclusion size unknown.
[m] Requires early stage of exchange, possibly while protoCAI was molten.
[**] Does not account for the presence of a fluid phase that would make the exchange more efficent.
[t] Inferred (not seen in the inner most WL rim).
[RM] Near 1000 K, equilibration times exceed 10^6 years regardless of the dislocation density within melilite (Ryerson and McKeegan, 1994).

within ~300 μm of the edge averages -0.9 ± 1.0‰ ($n = 13$, Traverse 1, unrimmed squares) and -2.6 ± 0.8‰ ($n = 7$, Traverse 2, squares with black borders). These values near the edge are within error of each other but differ slightly from some melilite toward the core. Melilite beyond ~300 μm from the inclusion edge exhibits a relatively constant $\Delta^{17}O$ of -0.1 ± 2.3‰ ($n = 4$) along Traverse 1, but it is slightly more ^{16}O-rich as measured by the longer Traverse 2, exhibiting an average $\Delta^{17}O$ value of -5.6 ± 0.6‰ ($n = 8$). Although the individual measurements are again mostly within error of each other, the apparent difference may reflect small differences in secondary mineralization along the two traverses, as a result of the fact that Traverse 1 crosscuts several more veins of secondary minerals than Traverse 2. The average $\Delta^{17}O$ value of fassaite within the melilite mantle is -18.2 ± 2.6‰ ($n = 4$, three are >700 μm from the edge, off scale in Fig. 9B) and that of spinel from the mantle and core is -24.7 ± 1.8‰ ($n = 9$). Primary anorthite exhibits $\Delta^{17}O$ values of −5‰ and −12‰ (locations are off scale in Fig. 9B), bracketing the slightly ^{16}O-enriched melilite compositions measured further toward the interior along Traverse 2. Veins and patches of secondary plagioclase replacing material between the WL rim and melilite at the edge of the interior along Traverse 1 have $\Delta^{17}O$ values ranging from −1.3‰ to 2.4‰ ($n = 3$), similar to that of adjacent melilite.

3.2.1.3. TS4. Two traverses across the margin of the Type B2 inclusion TS4 (Fig. 9C) were accompanied by analyses of fassaite, spinel, and anorthite from further within the interior. Melilite within ~500 μm of the edge has an average $\Delta^{17}O$ value of -0.5 ± 0.7‰ ($n = 16$), whereas melilite further inward has $\Delta^{17}O$ values that range from −4‰ to −5‰ ($n = 3$). Fassaite within the outermost ~300 μm has an average $\Delta^{17}O$ value of -22.1 ± 2.1‰ ($n = 6$), indistinguishable from that of fassaite further within the interior, with an average $\Delta^{17}O$ value of -22.3 ± 1.3‰ ($n = 6$). Spinel within the interior has an average $\Delta^{17}O$ value of -22.3 ± 1.5‰ ($n = 9$), indistinguishable from that of fassaite (Fig. 9C). Interior anorthite analyses yield $\Delta^{17}O$ values that range from −11‰ to −3‰ ($n = 4$), similar to, or possibly, slightly more ^{16}O-enriched than melilite compositions also measured >500 μm from the edge.

3.2.1.4. L6. Three NanoSIMS traverses were measured across the melilite margin of this compact Type A inclusion (Fig. 9D). The most negative $\Delta^{17}O$ values (−20‰, $n = 2$) occur at the outermost edge of Traverse 3, and intermediate values (between −15‰ and −10‰, $n = 5$) occur inward along Traverse 3 and within Traverse 1. The remaining measurements, starting ~100 μm from the edge to ⩾500 μm inward, including data from Traverses 1 and 2 that represent the bulk of the interior melilite, show no obvious zoning and exhibit an average $\Delta^{17}O$ value of -6.9 ± 1.5‰ ($n = 28$). The O-isotopic zoning profile in this CAI and those observed in the remaining inclusions are different from those discussed above. Such trends of increasing ^{16}O enrichment outward are referred to as "reverse" oxygen isotopic zoning in this work.

3.2.1.5. ALH3. A traverse across the outer margin of compact Type A inclusion ALH3 and interior melilite spots positioned at the ends of three additional traverses focused on its WL rim were measured (Fig. 9E). Melilite at the inclusion edge and within the outermost 100 μm of this traverse (diamonds) has an average $\Delta^{17}O$ of -7.7 ± 1.4‰ ($n = 6$), whereas melilite located >100 μm inward exhibits an average $\Delta^{17}O$ value of -5.2 ± 1.5‰ ($n = 7$). When analyses of melilite near the WL rim/interior boundary from the other traverses are included, the average $\Delta^{17}O$ within the first <100 μm drops slightly to a value of -8.3 ± 1.1‰ ($n = 11$), which appears distinct from the interior. The $\Delta^{17}O$ values of secondary minerals in ALH3 are not shown in Fig. 9E, but are near zero, distinct from those of adjacent, primary melilite.

3.2.1.6. Ef-1. The traverse across the margin of Ef-1 also shows a reverse sense of O-isotopic zoning (Fig. 9F). Melilite within 100 μm of the edge of Ef-1 exhibits an average $\Delta^{17}O$ value of -5.0 ± 1.6‰ ($n = 8$), whereas the interior is slightly less ^{16}O-rich ($\Delta^{17}O = -1.9 \pm 1.3$‰, $n = 6$). A single interior spinel grain is much more ^{16}O-rich, $\Delta^{17}O = -21$‰, than any of the interior melilite.

3.2.2. Isotopic heterogeneity among Wark–Lovering rim layers

In all of the CAIs studied, the WL rims exhibit extreme O-isotopic heterogeneity (up to ~25‰), whether the interiors are normal or reversely zoned. In most cases, the WL rims exhibit changes in $\Delta^{17}O$ over small spatial scales, e.g., ⩽10 μm. Results are illustrated in Fig. 10. Data for multiple traverses are plotted together. In order to account for local differences in layer thickness between traverses, offsets to the absolute positions of some analyses have been made to eliminate the appearance of mineral mixing. To accurately show intra-layer zoning, however, no adjustments were made within individual traverses on a given mineral layer.

3.2.2.1. A37. No new measurements were performed on the rim of this compact Type A inclusion; data shown in Fig. 10A are from Simon et al. (2011). The WL rim is ~50–100 μm thick and consists of a layered mineral sequence, from the interior outward, of hibonite ± melilite, spinel (enclosing perovskite), melilite/nepheline, pyroxene grading outward from Ti-bearing to Al-rich diopside, and an outermost layer of olivine (Fig. 4C). The melilite at the edge of the inclusion has an average $\Delta^{17}O$ value of -2.2 ± 3.0‰ ($n = 6$). Considerations of its distinct sodium abundance and texture (Fig. 4D) led Simon et al. (2011) to suggest that this melilite may represent the initial stage of rim formation. Hibonite yields a $\Delta^{17}O$ value of −17‰ that is indistinguishable from that measured in neighboring perovskite enclosed within spinel. Spinel yields an average $\Delta^{17}O$ value of -23.1 ± 1.4‰ ($n = 15$). The pyroxene layer exhibits reverse O-isotopic zoning, where the inner pyroxene has $\Delta^{17}O$ up to −6‰ and the outer pyroxene has an average $\Delta^{17}O$ value of -20.9 ± 1.8‰ ($n = 7$) (Fig. 10A). The innermost portion of the pyroxene layer lies in direct contact with a ~10–20 μm layer of melilite + nepheline

(incorrectly identified as sodalite by Simon et al., 2011) that has a planetary-like O-isotopic composition. The olivine layer exhibits a wide range of $\Delta^{17}O$ values, from −24‰ to −6‰. Backscattered electron images reveal localized, less forsteritic regions of olivine, and on average, the relatively FeO-rich olivine tends to have slightly higher and less variable $\Delta^{17}O$ (values range from −16‰ to −9‰).

3.2.2.2. Egg-6. This Type B1 inclusion, with relatively ^{16}O-poor, nearly isotopically homogeneous melilite, is surrounded by a simple, two-layer, spinel-pyroxene WL rim sequence (Fig. 6). The FeO content of the spinel increases outward; innermost, magnesian spinel contains discontinuous lenses of Ti-rich pyroxene and isolated perovskite (Fig. 6B and C). A NanoSIMS traverse across the rim starts near the outer point of Traverse 2, within the interior, and continues across the rim (Fig. 10B). Analyses were also made of aluminous diopside, spinel, and perovskite enclosed in the spinel layer. Ti-rich pyroxene has $\Delta^{17}O$ values that range from −4‰ to −2‰ ($n = 2$), indistinguishable from most perovskite. Three of the four perovskite grains analyzed have $\Delta^{17}O$ values of −4‰ to −1‰; the outermost perovskite grain has a $\Delta^{17}O$ value of −10‰. The outer, diopside layer exhibits reverse O-isotopic zoning, with the innermost spot having $\Delta^{17}O$ of −4‰ and the outer spot a $\Delta^{17}O$ value of −13‰. Ti-rich pyroxene grains enclosed in the spinel layer are notably ^{16}O-poor compared to both the outer part of the diopside layer and the Ti-rich pyroxene in the interior of the CAI.

3.2.2.3. TS4. This Type B2 inclusion has relatively ^{16}O-poor, isotopically homogeneous melilite in its interior and is surrounded by a ~15–60 μm thick WL rim composed, from interior outward, of spinel, Ti-bearing pyroxene grading into aluminous pyroxene, and a thick, semi-continuous layer of olivine that underlays the accretionary olivine rim (Fig. 7B). The discontinuous outer region of sodalite and patches of secondary plagioclase that occur just inside of, and are partially intermingled with, the spinel layer exhibit near-zero $\Delta^{17}O$. The interface between the ~10 and 25 μm thick spinel layer and interior spinel can be difficult to define in this sample, but spinel at the interior's edge has a $\Delta^{17}O$ value of −20‰, similar to spinel in the interior and less ^{16}O-rich than observed in some other CAI rims (e.g., Egg-6). Analysis of the ~5 μm-thick, zoned pyroxene layer yields a $\Delta^{17}O$ of −6‰ (Fig. 10C). The ⩾30 μm thick, outer olivine layer is heterogeneous in O-isotopic composition, exhibiting $\Delta^{17}O$ values ranging from −20‰ to 0‰. Normal isotopic zoning is observed within the coherent olivine layer, as analyses within ~25 μm of the pyroxene layer exhibit $\Delta^{17}O$ values that range from −21‰ to −6‰ ($n = 4$), whereas the remaining measurements closer to the matrix range from −5‰ to 0‰ ($n = 3$), indistinguishable from a measurement in the accretionary rim that has a $\Delta^{17}O$ value of 0‰.

3.2.2.4. L6. This minimally altered compact Type A inclusion is surrounded by a continuous and locally thick (up to 100 μm) layer of spinel intergrown with melilite, with reverse O-isotopic zoning at the edge of the melilite interior. As shown in Fig. 10D, spinel grains have an average $\Delta^{17}O$ value of −24.9 ± 1.2‰ ($n = 8$). In the innermost chemically zoned melilite layer(s) that includes Mel-1 and Mel-2 (Fig. 8B), $\Delta^{17}O$ is −4‰ ($n = 3$), but $\Delta^{17}O$ in melilite in the outer spinel-melilite layer (Mel-3), varies from −5‰, like a majority of interior melilite, to −26‰. Diopside in Al-pyx-5, the outermost layer, has $\Delta^{17}O$ values ranging from −14‰ to −22‰ ($n = 4$), and averages −18‰. Among the pyroxene layers, $\Delta^{17}O$ increases inward from Al-pyx-5, to Ti-pyx-4, with an average of −17‰, to Ti-Pyx-3, with an average of −13‰, to Ti-pyx-1, at −10‰.

3.2.2.5. ALH3. This compact Type A inclusion has subtle, reverse O-isotopic zoning in the interior. The primary WL rim traverse reflects a continuation of Traverse 4, originating from the interior. Additional WL rim analyses come from a sub-parallel traverse (#3) ~20 μm away and a pair of traverses (#1 and #2) across a WL rim sequence lining the bottom of an embayment, located at the edge of a matrix pocket within ALH3. Spinel yields an average $\Delta^{17}O$ value of −22.0 ± 1.9‰ ($n = 7$) (Fig. 10E), while pyroxene measurements are more variable, averaging −11.0 ± 5‰ ($n = 7$). There is evidence for reverse zoning across the pyroxene (Fig. 10E), where $\Delta^{17}O$ values increase inward across two separate traverses, from −22‰ to −4‰ and from $\Delta^{17}O = -11$‰ to −7‰. The pyroxene analyses with the highest ^{16}O abundances along each traverse are those furthest away from the spinel layer. All measured olivine lies within an ~20 μm-thick layer at the interface between the WL rim and the matrix. Olivine yields $\Delta^{17}O$ values of −26‰, −25‰, −11‰, and 0‰; the two ^{16}O-rich analyses come from the same grain.

3.2.2.6. Ef-1. This minimally altered compact Type A inclusion is surrounded by a simple, two-layer, spinel-pyroxene WL rim sequence, with a melilite interior exhibiting reverse O-isotopic zoning. Two analytical traverses transect the rim (Fig. 10F). The spinel layer, ~5–10 μm thick and interfingered with the margin of interior melilite, has an average $\Delta^{17}O$ value of −21.4 ± 3.2‰ ($n = 4$), similar to that of interior spinel. The pyroxene layer is ~10–15 μm thick and chemically zoned from Ti-rich to aluminous diopside. A single traverse across the pyroxene layer reveals reverse O-isotope zoning, from a $\Delta^{17}O$ value of −11‰ near the ^{16}O-rich spinel layer and −20‰ near the contact with the fine-grained, olivine-dominated matrix, which has a $\Delta^{17}O$ of −1.6 ± 5‰ ($n = 4$). No secondary mineralization was observed in the WL rim of this inclusion (Fig. 2).

4. DISCUSSION

4.1. Characteristics of oxygen isotopic exchange in the interiors and rims of CAIs

A number of processes can be envisioned that can potentially explain the heterogeneous distribution of O-isotopic compositions in the interiors and WL rims of CAIs (e.g., Clayton et al., 1977; Ryerson and McKeegan, 1994; Yurimoto et al., 1998; Yoshitake et al., 2005; Aleon et al., 2007; Simon et al., 2011; Park et al., 2012). Exchange

between a molten CAI with an ^{16}O-rich protosolar composition and a gaseous reservoir with a planetary, relatively ^{16}O-poor isotopic composition could occur rapidly, before any crystals form, or more slowly, while the CAI crystallizes. The first case would produce a CAI in which all minerals have a uniform, relatively ^{16}O-poor, planetary-like O-isotopic composition. This is never observed. The second case would yield a CAI in which Δ^{17}O is lowest in spinel, the phase with the highest crystallization temperature, highest in pyroxene and anorthite, the solidus phases, and intermediate in melilite. This is also never observed. An alternative scenario could involve O-isotopic exchange between a solid CAI of protosolar O-isotopic composition and a near-zero Δ^{17}O planetary oxygen reservoir on the chondrite parent body. This parent body scenario would yield progressively less negative Δ^{17}O values in melilite from the center of the CAI to the edge, which is seen only in some CAIs (e.g., Egg-6). A parent body scenario would also likely lead to less negative Δ^{17}O values from the inside out within a given mineral layer and between similar phases from the inner to the outer rim, which was not observed in this study. For CAI interiors, the remaining possibility is exchange between solid CAIs of protosolar O-isotopic composition and several nebular gas reservoirs with distinct O-isotopic compositions. It should be noted that some interactions could have occurred between nebular gas and inclusions in which both had similar isotopic compositions. In this case the solid–gas interaction would leave little to no isotopic record. It is also possible that some WL rim growth involved a non-solar gas with a protosolar O-isotopic composition. For rim layers, the remaining possibility is growth of different layers from distinct nebular reservoirs, most dramatically indicated by reversals in the gradients of isotopic compositions observed in the present work.

Despite the wealth of O-isotopic measurements of CAIs, only a few studies have systematically addressed, at high spatial resolution, the radial distribution of O-isotopes in CAIs and their rims. In examples that do exist, including those reported herein, there are some general features that provide important diffusion model input parameters and allow us to make specific predictions for environment(s) from which CAIs formed and evolved. Illustrative model results shown in Table 4 include examples of complete oxygen exchange between protosolar and near planetary compositions for a variety of end-member cases ("Idealized CAIs") involving molten objects at 1773 K or 1973 K and 1 bar; solid objects with no defects at 1400 K and $P^{tot} = 10^{-3}$ bar and 1500 K and $P^{tot} = 10^{-2}$ bar; and solid objects with significant lattice dislocations, both large (2 cm) and smaller (0.5 cm) CAI sizes, at 1400 K and 1500 K, respectively. Table 4 also summarizes results that reflect the timescales for diffusive exchange to reproduce the isotopic compositions characteristic of the interiors and the external isotopic reservoirs implied by the "Studied CAIs" for nebular and planetary scenarios. These models assume mean temperatures (pressures) of 1400 K ($P^{tot} = 10^{-3}$ bar) and 900 K (1 bar), respectively. Representative diffusion models are compared to the isotopic zoning profiles in the interiors of the inclusions and shown in Fig. 9. Although such models are non-unique, a comparison between the model curves and the measured profiles can be used to determine plausible temperature-dependent timescales of O-isotopic exchange in the CAIs, and ultimately used to constrain the possible environments where exchange occurred, i.e., nebular (Shu et al., 2001; Cuzzi et al., 2003; Boss et al., 2012) or on a planetary body (Wasson et al., 2001).

Model curves were computed to reflect the exchange of O-isotopes in each CAI to investigate the possibility that the Δ^{17}O profiles developed following crystallization, assuming each CAI subsequently exchanged oxygen with a reservoir of distinct O-isotope composition. It is possible that the progress of isotopic exchange due to reheating occurred in numerous short (hours to days) events within the solar nebula (e.g., Young et al., 2005). None of these isothermal models reproduce actual heating events, but allow assessment of the plausibility of exchange by solid-state diffusion. Based on the broad trends and relative lack of localized O-isotopic heterogeneity observed across the melilite interiors of the studied inclusions, the models summarized in Table 4 are those that consider diffusion length scales at the inclusion scale rather than the individual mineral grain scale. To model the profiles observed in L6, Ef-1, and ALH3, the CAIs exhibiting relatively ^{16}O-poor interiors with melilite margins that are comparatively ^{16}O-rich (i.e., exhibit reverse zoning), starting conditions for a second step of isotopic exchange assumed an interior that was previously enriched in "heavy" oxygen and uniformly ^{16}O-poor, −5‰, 0‰, and −3‰, respectively. More complicated models, where the distribution of O-isotopes within the interior is non-uniform, e.g., like in A37, would be necessary to fully understand the timescales and temperatures required to explain the reversely zoned profiles. Models that match the relatively ^{16}O-poor and nearly uniform melilite profiles of the Type B inclusions (Egg-6 and TS4) are shown in Fig. 9 although it is debatable whether a nebular process provides the best explanation for the O-isotopic compositions of their melilite.

The individual models for the inclusions do not take into account enhanced-diffusivity due to crystal lattice dislocations (Ryerson and McKeegan, 1994), fast diffusion pathways along grain boundaries, or the presence of a fluid phase. Dislocations in minerals contained in CAIs are generated by exposure to ionizing radiation emitted from the protoSun, and their density increases with exposure time (Kwok et al., 1978). For example, in an Allende CAI Barber et al. (1984) found dislocation densities $<10^8$/cm^2 in spinel and pyroxene and $\sim10^9$/cm^2 in melilite. Ryerson and McKeegan (1994) calculated that equilibration of oxygen isotopes in melilite at temperatures approaching the solidus (~1500 K) would happen within years, an order of magnitude faster than in dislocation-free grains (see "Idealized CAIs" with "defects" included in Table 4). On the other hand, Ryerson and McKeegan (1994) find that equilibration times exceed 10^6 years regardless of the dislocation density within melilite at temperatures relevant to chondrite parent bodies (e.g., <1000 K). It follows that significant isotopic zoning like that seen within the melilite interiors of A37 and L6 should be rare. Therefore these rare inclusions possibly indicate rapid accretion onto a parent body, as an inclusion with significant dislocations would likely be efficiently homogenized in the nebula, leading to

the relatively homogeneous melilite interiors documented in other CAIs.

4.2. Effect of parent body alteration on oxygen isotopes of refractory inclusions

Inclusions in Allende, Efremovka, and Leoville contain evidence of secondary alteration. This alteration is largely due to hydrous fluids or gas, assisted by heating in asteroidal and nebular environments (Brearley, 1997; Hutcheon et al., 1998; Huss et al., 2006, and references therein). The effect of water on intra-mineral (volume) diffusion is a subject of debate, but it likely enhances exchange rates at parent body temperatures, but apparently not significantly at nebular ones (>1000 K), e.g., Ingrin et al. (2001) and Ryerson and McKeegan (1994). Noble gas data indicative of the abundance and survival of presolar grains (Huss et al., 2003) and Raman spectroscopic studies of organic material (Bonal et al., 2006) suggest that CV3 meteorites experienced moderate peak temperatures, ~500–900 K, during parent body processing (Huss et al., 2006). The timescale for producing these peak temperatures, e.g., ⩽800 K on the Allende parent body, primarily reflects parent body size and the initial abundance and subsequent decay of ^{26}Al (i.e., $^{26}Al/^{27}Al_0 = 3–5 \times 10^{-6}$). Young (2001) and Kunihiro et al. (2004) estimate that it would take more than 2×10^6 years to reach these peak temperatures and that they would not persist for more than 5×10^5 years. Other potential sources of heat include magnetic induction and impacts (Rubin, 1995), although neither induction nor collisional heating are likely to result in the relatively high temperatures required by the global thermal metamorphism of chondrite parent bodies (Keil et al., 1997). The timescale of radiogenic heating is incompatible with the magnitude of O-isotope exchange inferred for the studied CAIs, as unrealistically long periods of time, ~10^6–10^8 years, would be required (Table 4; Yurimoto et al., 1989; Ryerson and McKeegan, 1994; Ingrin et al., 2001).

If the O-isotopic profiles in the interiors of CAIs were established by incomplete exchange with a planetary isotopic reservoir, it is noteworthy that there are larger shifts within the melilite in Ef-1 and L6, both from reduced CV3 chondrites, than in A37, from an oxidized CV3 chondrite. Moreover, much of the melilite in the Type A CAI interiors appears to be "lighter" than typical bulk O-isotopic compositions of inclusions from CV3 chondrites. Additionally, L6, ALH3 and EF-1 record O-isotopic gradients within their interiors that exhibit relative ^{16}O-enrichment trends toward their edges. Although sometimes subtle, this "reverse" zoning is not consistent with late parent body exchange because the latter would produce "normal" zoning. Collectively, these observations argue that the primary process(es) responsible for incorporating relatively ^{16}O-poor oxygen into the CAI interiors occurred in the nebula rather than the parent body. Finally, the O-isotopic heterogeneity within the rim layers surrounding the CAIs, and especially the presence of the relatively ^{16}O-rich, fine-grained (i.e., high surface area) melilite in the Wark–Lovering rim of L6 provides strong evidence that some coarse-grained melilite in the CAI interiors became relatively ^{16}O-poor prior to rim formation.

Among the CAIs studied here, it is also noteworthy that the evidence for isotopic exchange is largely uncorrelated with the degree of secondary alteration discernible from petrographic study. This can be clearly seen by the fact that both A37, whose interior records only "normal" isotopic exchange, and L6, with an interior that records "reverse" zoning and which likely had a much more complex and evolved isotopic exchange history than A37, contain minimal amounts of secondary alteration products. It is therefore concluded that the visibly unaltered primary mineral assemblages within many CAIs experienced minimal O-isotopic exchange on their parent bodies.

4.3. Nebular isotopic exchange with CAI interiors

4.3.1. A37

The interior of this inclusion is "normally" zoned, with Δ^{17}O values in melilite increasing monotonically from -17.5 ± 0.8‰ ($n = 20$) in the interior to -2.2 ± 3.0‰ ($n = 6$) at the inclusion edge (Fig. 9A). New spinel analyses in the present study from the interior of A37 are significantly more ^{16}O-rich ($\Delta^{17}O \sim -29$‰) than both the new and previously reported interior melilite data (Simon et al., 2011). A similar oxygen diffusion model was employed in that work as in the present study but, since previously no interior spinel had been measured, Simon et al. (2011) concluded that a single-step, solid-state diffusion model could explain the O-isotopic profile of A37. The new spinel data (Fig. 9A), however, have the usual protosolar Δ^{17}O of ~−29‰, indicating the likelihood that the entirety of the A37 interior formed initially with this Δ^{17}O value. The red curve in Fig. 9A is representative of the mismatch of single-step models for A37. All such temperature–time models that reproduce the relatively elevated ~−18‰ value of the interior yield too shallow a curvature to be considered a good match to the data. More likely, A37 experienced an early oxygen exchange event that reset melilite to an intermediate Δ^{17}O value (step 1), the relatively uniform value measured in the interior, before melilite at its margin exchanged further with a near-zero Δ^{17}O planetary reservoir (step 2). The black curves in Fig. 9A represent a family of two-step diffusion models with temperature–time parameters of 1400 K and $\sim 2 \times 10^4$ years in step 1 and 1400 K and $\sim 1.6 \times 10^4$ years for step 2, which yield a good match to the measurements. Although elevation of the Δ^{17}O value in interior melilite by ~10‰ relative to the spinel could be due to exchange while the CAI was partially molten, exchange that led to the measured zoning profile can only be fit at subsolidus temperatures.

4.3.2. Egg-6 and TS4

Interior melilite in Type B CAIs Egg-6 and TS4 differs from that in the Type A CAIs of this study in having near-zero Δ^{17}O values at their margins and nearly uniform and relatively high values, mostly between 0‰ and −5‰, throughout the rest of their interiors (Fig. 9B and C). Assuming that all CAIs started with protosolar, ^{16}O-rich

compositions, these values indicate nearly complete exchange with a relatively ^{16}O-poor reservoir in the solid-state. The melilite interiors of both Type B CAIs can be matched with single-step models (e.g., black curves in Fig. 9B), but TS4 appears to require at least two-steps (Fig. 9C) as discussed below. A diffusion model for Egg-6 with temperature–time parameters of 1400 K and $\sim 2.8 \times 10^5$ years yields a good match to the subtle gradient exhibited by melilite and anorthite measurements that comprise Traverse 2 (bold curve in Fig. 9B). A similar model shown by the upper thin black curve run for 3.0×10^5 model years passes through all of the Egg-6 melilite, including those in Traverse 1 that are suspected to reflect some contamination by secondary mineralization.

In Egg-6, fassaite has higher Δ^{17}O, ~ -18‰, than spinel, ~ -25‰, while, in TS4, these phases have nearly equal Δ^{17}O values of ~ -22‰, rather elevated compared to the protosolar value. Explaining the difference between fassaite and spinel in Egg-6, or the lack thereof in TS4, by a single subsolidus diffusion process or heating event is difficult. The difference in O-isotopic composition between spinel, fassaite and melilite in Egg-6 likely reflects differential subsolidus exchange with a relatively ^{16}O-poor reservoir, whereby fassaite exchanged more thoroughly than spinel, and melilite more extensively than fassaite, as suggested originally by Clayton et al. (1977). This could have happened on the parent body or in the nebula. Despite abundant evidence for remelting in Type B CAIs it is unlikely that the preferential incorporation of "heavy" oxygen in melilite occurred while the inclusion was partially molten because we know from experimental phase equilibria that the pyroxene would have crystallized after most of the melilite (Stolper, 1982).

Because fassaite and spinel have distinct oxygen diffusivities, their similar but elevated Δ^{17}O values suggest that TS4 exchanged thoroughly with a nebular gas reservoir with $\Delta^{17}\mathrm{O} \approx -20$‰, intermediate between the protosolar and planetary values. This exchange could have happened while the inclusion was a melt (in hours to days) or in the solid-state (Table 4). Model curves (Fig. 9C) reflect two-steps of exchange, with the intermediate Δ^{17}O value recorded by spinel and fassaite interpreted to have preserved the shift from the protosolar Δ^{17}O value (step 1), before melilite exchanged further with a planetary Δ^{17}O value (step 2). It is notable that the intermediate composition modeled by step 1 is similar to that of spinel in the rims of Type A CAIs Ef-1, A37, and E49 of Aleon et al. (2007), and most of the melilite in the interior of A37. Both steps of exchange may have occurred prior to formation of the WL rim, whose innermost spinel is much more ^{16}O-rich (Fig. 10C). Representative diffusion models with temperature–time parameters of 1400 K and $\sim 2 \times 10^4$ years in step 1 and 1400 K and $\sim 3 \times 10^4$ years for step 2 yield an acceptable match to the measurements (black curves in Fig. 9C).

4.3.3. L6

The outer margin of this inclusion is "reversely" zoned, with Δ^{17}O values in melilite decreasing monotonically from a relatively uniform value of ~ -7‰ in the interior to ~ -20‰ at the margin (Fig. 9D). For reversely zoned CAIs, the model curves were calculated in two steps as above, except that in the second step the interior melilite values were used for the initial CAI value and the nebular gas reservoir was assumed to have the same Δ^{17}O as the spinel in the WL rims (see Table 4). Assuming that the L6 precursor grew originally from a relatively ^{16}O-rich protosolar gas, a majority of its melilite interior later exchanged with a reservoir having a relatively ^{16}O-poor composition (step 1). A diffusion model with temperature–time parameters of 1400 K and $\sim 3 \times 10^4$ years approximates the Δ^{17}O of its melilite interior (Table 4). In detail, the representative model listed in Table 4 is run long enough to produce an interior value that exceeds the uniform value of ~ -7‰ in the interior because the extent of subsequent exchange needed (in step 2 below) to produce the rather extreme ^{16}O-enrichment (-20‰) at the edge would drop the modeled -5‰ interior value back down to the measured value of the interior (~ -7‰). Based on the match of the model diffusion profile to the O-isotopic composition of the melilite observed at the edge of the inclusion, L6 likely experienced a second exchange event (step 2) that exposed the relatively ^{16}O-poor interior to a relatively ^{16}O-rich nebular gas, a process that would have taken $\sim 2.6 \times 10^4$ years at 1400 K (Table 4). The L6 profile, and the isotopic composition of its interior and rim spinel ($\Delta^{17}\mathrm{O} \sim -20$‰ to -25‰) are very similar to those of E49 (Aleon et al., 2007), and both inclusions may have had similar formation histories.

4.3.4. Ef-1 and ALH3

In contrast to the near-zero Δ^{17}O values measured at the margins of A37 and the Type B CAIs, Ef-1 and ALH3 exhibit relative ^{16}O-enrichments at their melilite margins with average Δ^{17}O values of -8 ± 1‰ ($n = 11$), and -5 ± 2‰ ($n = 8$), respectively (Fig. 9E and F). Although less extreme than the $\Delta^{17}\mathrm{O} \sim -20$‰ measured at the margin of L6, these reversals in O-isotopic zoning profiles also imply two exchange events. The interiors of both CAIs record an event that transformed their assumed protosolar starting compositions into relatively ^{16}O-poor compositions (step 1), followed by exposure to a more ^{16}O-rich nebular gas, producing the higher ^{16}O abundances at the CAI margins (step 2). Diffusion models with temperature–time parameters of 1400 K and 10^3 years and 1400 K and 1.9×10^4 years, approximates the Δ^{17}O of their respective melilite interiors (step 1's). Because the CAIs are rather large (originally $\geqslant 0.5$ cm) even the slight ^{16}O-enrichements detected at the margins of Ef-1 and ALH3, require relatively long exposure times, 5×10^3 and 1.9×10^4 years, respectively (step 2's). The higher melting temperature of the gehlenitic melilite composition characteristic of ALH3 permits subsolidus model temperatures higher than 1400 K. In these relatively high temperature calculations modeled exchange in ALH3 could be up to ~ 5 times faster.

In general, the modeled timescales for O-isotope exchange are comparable to those reported by Simon and Young (2011), based on the Mg-isotope profiles in coarse-grained CAIs. Unlike spinel, in which oxygen diffuses much more slowly than magnesium, oxygen diffusivities in melilite are only slightly lower than magnesium diffusivities (LaTourrette and Hutcheon, 1999; Simon and Young,

2011, and references therein). Based on this complementarity, it follows that a majority of the oxygen data reported herein and the magnesium data reported for similar inclusions (e.g., Fahey et al., 1987a; Simon et al., 2005; Simon and Young, 2011; Bullock et al., 2013) from CV3 chondrites imply early, open-system exchange, and resetting in the solid-state (Fahey et al., 1987b; Simon and Young, 2011; Simon et al., 2005; Young et al., 2005), which could reflect a common early solar system reprocessing event and/or environment.

4.4. Nebular scenarios implied by the oxygen isotopic records of Wark–Lovering rim layers

As first suggested by Wasserburg et al. (1977) and confirmed by Cosarinsky et al. (2005) and Simon et al. (2005), at least some WL rims formed within 10^5 years of CAI crystallization. Three mechanisms are frequently invoked to explain part or all of their formation: (1) "flash heating", whereby inner layers formed by melting and/or evaporation during intense heating (Boynton and Wark, 1985; Wark and Boynton, 2001); (2) "subsolidus deposition", whereby outer layers formed sequentially by condensation during cooling and/or vapor deposition due to an increased gas pressure or changing composition (Wark and Lovering, 1977; Fahey et al., 1987b; Simon et al., 2005); and (3) growth due to "chemical potential gradients", where the common mineral layer sequence of spinel ± hibonite→melilite→pyroxene→olivine was produced simultaneously by metasomatic reaction with nebular gas (Wark and Lovering, 1977; MacPherson et al., 1981; Ruzicka, 1997) or from elements in the gas phase alone (Simon et al., 2005). The O-isotope variability in WL rims, discussed next, demonstrates that growth occurred from distinct gas reservoirs, that gas chemistry contributing to mineral growth and potentially leading to higher more planetary f_{O_2}, can be decoupled from gas isotopic compositions, and that, similar to the interiors, the initial O-isotope composition of some rim layers may have been later modified by exposure to distinct gas reservoirs.

Several important observations can be made from the present work: (1) pyroxene found in WL rims tends to exhibit reverse O-isotopic zoning. That is, when multiple analyses were made, either within a single layer or among the multiple pyroxene layers surrounding L6 and Egg-6 (Fig. 10) the outermost spots (i.e., those located closer to the matrix) tend to be relatively ^{16}O-rich. This observation is difficult to explain by simple mixing between oxygen originally contained in the inclusion and any near-zero Δ^{17}O oxygen reservoir; (2) For two CAIs (A37, L6), O-isotopic compositions at the edges of their melilite interiors and the innermost layer of the WL rims are similar—possibly implying a genetic relationship. In an analogous way, the melilite interiors of the other two Type A CAIs (ALH3, Ef-1), which exhibit more subtle O-isotopic gradients, may record a signature of edgeward ^{16}O-enrichement related to WL rim formation. In contrast, the O-isotopic compositions of melilite observed in the two Type B CAIs (Egg-6, TS4) contain little to no evidence of a relationship with their WL rims, the exception being that in Egg-6, the pervoskite and pyroxene enclosed in spinel in the rim have compositions similar to melilite at the edge of the interior; (3) spinel found in WL rims typically has compositions that are slightly less ^{16}O-rich compared to the protosolar gas composition (Fig. 10), but with measurable differences among the various CAIs not readily attributable to secondary alteration. Differences among WL rim spinel compositions could have been derived from initially protosolar spinel that was cogenetic with CAI interiors (Wark and Lovering, 1982) and incrementally exchanged when the next layer, e.g., relatively ^{16}O-poor melilite and/or pyroxene, was deposited; or they may reflect early rim deposition from gas reservoirs with distinct O-isotopic compositions; and (4) O-isotopic differences between adjacent zones require that some mineral layers formed sequentially, rather than contemporaneously as hypothesized by some models in which large chemical potential gradients drove their formation (e.g., Ruzicka, 1997). The measured isotopic heterogeneity over short length scales is inconsistent with the standard metasomatic mechanism, which would have likely resulted in a continuous isotopic gradient because such a model implies that the more refractory elements were scavenged from the interior and diffusively exchanged with material that was added at the surface. It is still possible that the WL rim layers grew under a chemical potential gradient (as, for example, suggested by Simon et al., 2005), but in such a scenario they condensed directly from the gas and formed from several gas reservoirs with isotopically distinct compositions.

4.4.1. The interface between WL rims and CAI interiors

In most CAIs, spinel defines the boundary between the outer edge of the interior and the innermost rim layer. It is unclear whether all of the spinel at the edge of an inclusion is part of the rim or not; some probably formed in the interior, as, for example, suggested by Wark and Lovering (1982). An exception to the rule is the existence of the innermost melilite and hibonite layer, "below" the spinel layer, in the WL rim surrounding A37 (see Fig. 4C and D and supplemental material of Simon et al., 2011). In this case, new melt at the inclusion edge might have lost Mg, and new, more gehlenitic melilite, precipitated on the underlying melilite interior, producing the observed sequence of melilite-on-melilite. This melt could be cogenetic with the spinel-perovskite layer, but its distinct, relatively high Na content, and relatively ^{16}O-poor isotopic composition, makes this scenario unlikely. Simon et al. (2011) analyzed hibonite in the rim and found that it is relatively ^{16}O-rich ($\Delta^{17}O \sim -17‰$). The intermediate O-isotopic compositions observed in hibonite may reflect a reaction between the relatively ^{16}O-poor, Na-rich melilite at the edge of the interior (i.e., recording the inclusion's original exposure to relatively ^{17,18}O-rich nebular gas) and the relatively ^{16}O-rich nebular gas related to formation of the spinel-perovskite layer. Alternatively, if hibonite is relatively resistant to oxygen exchange compared to melilite, it may have been relatively ^{16}O-rich and only partially exchanged with the relatively ^{17,18}O-rich reservoir that exchanged with the interior.

4.4.2. Spinel layers

These layers in WL rims are relatively ^{16}O-rich, with Δ^{17}O values ranging from −30‰ to −18‰, with most values ⩽−20‰ (Figs. 9 and 10) and uniform in composition within a given rim. The possible exception is the spinel layer surrounding Egg-6. A comparison of X-ray image data and the O-isotope measurements show that its outermost spinel is more FeO-rich and slightly ^{16}O-poor compared to some more magnesian spinel closer to the CAI edge. Substitution of Fe for Mg in spinel often indicates parent body alteration and implies that the slight shift toward relatively ^{16}O-poor compositions in the outermost spinel zone could have happened on the parent body. The spinel layers surrounding A37, Egg-6, and L6 have average Δ^{17}O values of ∼−25‰ or less, whereas Ef-1, TS4, and E49 (Aleon et al., 2007) have Δ^{17}O values of −20‰. The possibility that O-isotopes in some Egg-6 spinel have been partially exchanged, and yet they are still more ^{16}O-rich than magnesian spinel in Ef-1, implies that Ef-1 spinel may have originated from a slightly ^{17,18}O-enriched reservoir. If the measured differences in Δ^{17}O of 5–10‰ among the studied inclusions reflect different degrees of O-isotope exchange upon pyroxene deposition, gradational variations within spinel layers might be expected, as in Egg-6. But evidence for differential exchange in spinel surrounding the other CAIs is lacking.

Based on comparison of trends in the O-isotopic zoning profiles and the compositions of the WL spinel layers (or melilite layer in the case of A37), rim formation may have affected the O-isotopic composition of the edges of the interiors of the studied Type A CAIs. In contrast, in both Type B inclusions studied here, there is no obvious connection between relatively ^{16}O-rich spinel in the rims and ^{16}O-poor melilite in their interiors. Nonetheless, with the possible exception of spinel in the WL rim surrounding Egg-6, the variability of the spinel data in both the most pristine (Ef-1 and L6) and most altered (TS4 and ALH3) inclusions provides evidence that the O-isotopic compositions of most WL rim spinel has little to nothing to do with secondary mineralization, rather, it likely grew and incorporated oxygen from different, possibly evolving nebular gas reservoirs.

4.4.3. Pyroxene layers

All WL rims contain a pyroxene layer. Most pyroxene appears to have formed in chemical disequilibrium with respect to the interior phases, implying later growth through metasomatic solid–gas reaction and/or condensation from a non-solar gas (Wark and Lovering, 1977; Ruzicka, 1997; Simon et al., 2005; Han and Brearley, 2012). The reverse O-isotopic zoning seen in the WL rim pyroxene layers surrounding Ef-1, A37, Egg-6, and ALH3 appears to be more common than normal zoning. The replicate sequences of pyroxene (and melilite) layers in L6, as well as the distinct O-isotopic compositions of the pyroxene, imply that, at least in this case, they likely formed sequentially rather than simultaneously.

At face value, the presence or lack of Ti^{3+} in the pyroxene layers can signify the state of oxidation during their growth. Redox conditions can be estimated by the equilibrium reactions of Simon et al. (2005), which relate the measured activities of pyroxene components, and estimated temperature and P_{SiO}/P_{Mg} in a coexisting nebular gas. Higher Ti^{3+}/Ti^{tot} due to the more reducing conditions expected during formation in a primitive nebular environment might be expected to correlate with greater ^{16}O abundance. In the case of the pyroxene layers surrounding L6, however, the innermost layer (Ti-pyx-1), with the highest Ti^{3+}/Ti^{tot} exhibits the lowest ^{16}O abundance, whereas the layer with the lowest measurable Ti^{3+}/Ti^{tot} has an intermediate Δ^{17}O value of −15‰. These results imply that the valence state of Ti and the O-isotopic composition of rim pyroxene are not always correlated, indicating a decoupling of the isotopic composition of the gas from other physicochemical parameters.

4.4.4. Melilite layers

This phase is absent from some WL rims. Where present, it is typically between the spinel and pyroxene rim layers and is often intergrown with plagioclase ± nepheline, which are likely products of alteration of the melilite. Exceptions include melilite at the interface with the interior of Allende A37, and the complicated WL rim surrounding L6 that contains three distinct occurrences of melilite. Often melilite in rims is relatively ^{16}O-poor, e.g., Ito et al. (2010) and Simon et al. (2011). This is the case for the inner sublayers "Mel-1, Mel-2" in the rim of L6 ($\Delta^{17}O = -4‰$). The fact that this melilite exhibits zoning in chemical composition (see Fig. 8B) but is homogeneous in O-isotopic composition indicates that there were more cycles of deposition than are recorded by isotopic differences.

In L6, the inner rim O-isotopic homogeneity contrasts sharply with the outermost occurrence of melilite (Mel-3), which exhibits O-isotopic heterogeneity, with Δ^{17}O values ranging from −26‰ to −5‰ (Fig. 10D). A single spinel analysis within the outermost melilite yields $\Delta^{17}O = -25‰$. The granular, relatively fine-grained texture of the outer melilite could indicate a period of accretion of individual melilite and spinel grains whose isotopic heterogeneity could have predated deposition, rather than formation *in situ*. Although the significance of this extreme variability is unclear, it is difficult to envision a scenario in which the fine-grained (i.e., high surface area) melilite in the outer layer retained its O-isotopic heterogeneity if the uniform, relatively ^{16}O-poor isotopic composition of the inner melilite layer(s) resulted from exchange of initially ^{16}O-rich melilite with a relatively ^{16}O-poor reservoir after formation of the outer melilite layer.

4.4.5. Olivine layers

At the outermost edges of WL rims, there are generally two types of olivine layers that can be distinguished texturally. Porous layers consisting of many individual crystals that tend to fill topographic depressions (clearly seen on TS4, Fig. 7A), are thought to be accretionary (MacPherson et al., 1985), and are not considered part of the WL rim in the present work. The outer melilite layer in L6 also has a porous, polycrystalline nature but is considered part of the WL rim because it is found inside massive, WL rim layers of pyroxene. The other type of olivine

occurs as thin but coherent, wall-like layers containing little pore space, and are interpreted here as WL rims that may have been vapor deposited (Simon et al., 2005; Keller et al., 2013). The heterogeneous O-isotopic compositions in the olivine rim layers of TS4 and ALH3 and in the accretionary rims of A37 suggest that both types of olivine had complex histories involving formation from relatively ^{16}O-rich and ^{16}O-poor gases (Krot et al., 2002). It is possible that the olivine in the WL rim, and its isotopic heterogeneity, reflects *in situ* condensation of olivine from a relatively ^{16}O-poor gas that is "peppered" with a previous generation of relatively ^{16}O-rich grains just prior to and/or as the earliest stage of accretionary rim formation. Elevated levels of FeO in both olivine types may be due to subsequent diffusive Fe–Mg exchange, and could have occurred without significant modification of the original O-isotopic composition of the olivine (Fagan et al., 2004b; Cosarinsky et al., 2008).

4.5. Mass-independent oxygen reservoirs in the early solar system

Δ^{17}O variability in the early solar system has been generally attributed to photodissociation of CO by self-shielding in the optically thin surface of the protosolar disk (Clayton, 2002; Lyons and Young, 2005; Sakamoto et al., 2007). This may have resulted in formation of relatively ^{17,18}O-rich water that spread heterogeneously throughout the disk where its oxygen was incorporated into silicates. Young (2007) suggested that this process occurs on a timescale of $\sim 10^5$ years. Alternatively, heterogeneous enrichment of ^{17,18}O may have existed very early in the history of the solar nebula originating from the parental molecular cloud (Yurimoto and Kuramoto, 2004; Dominguez, 2010).

In addition to the protosolar oxygen isotopic composition, $\Delta^{17}O \sim -25‰$ to $-30‰$, and the planetary values, $\Delta^{17}O \sim 0‰$ to $-5‰$, that are frequently encountered in CAI materials, another common composition in this study is $\Delta^{17}O \sim -17‰$ to 23‰. This intermediate composition is found in the fassaite and spinel in TS4, a majority of the melilite in the A37 interior, and spinel in the WL rim of Ef-1 in the present work, as well as in the CAI rim studied by Aleon et al. (2007). While the common occurrence of this value may be the fortuitous result of exchange between inclusions with a protosolar composition and an ^{16}O-depleted reservoir, it is also possible that there was a distinct reservoir of intermediate oxygen isotopic composition sufficiently widespread and long-lived to have left its imprint on all of these materials, analogous to that proposed for chondrules by Chaussidon et al. (2008).

4.6. Implications for protoplanetary disk environments and evolution

The extreme O-isotopic heterogeneity recorded by CAIs and their WL rims is consistent with exposure to nebular gases with different O-isotopic compositions. CAIs that formed in the inner solar system may have initially had relatively ^{16}O-rich "protosolar" compositions. Thermodynamic calculations show that, as the protoplanetary disk cooled, the refractory phases characteristic of CAIs would not have survived had they continued to equilibrated with the gas down to low temperatures (Grossman et al., 2002, 2008). Analyses of refractory cometary samples show that the solar nebula experienced a phase of large-scale outward transport of refractory grains (Brownlee et al., 2006) and that these grains are relatively ^{16}O-rich, similar to the $\Delta^{17}O \sim -20 \pm 3‰$ compositions of "normal" bulk CAIs (McKeegan et al., 2006; Krot et al., 2010; Bullock et al., 2012) and a possible "intermediate" oxygen isotopic reservoir envisioned herein. Likewise, there are a number of ways refractory inclusions could have been removed from the inner solar nebula. One way is by large-scale transport and mixing processes associated with a marginally gravitationally unstable disk, a likely cause of FU Orionis events in young low-mass stars, e.g., Boss et al. (2012). Protostellar jets and disk winds, commonly associated with star formation, have also been suggested (Shu et al., 1996). These hot winds may have played a role in heating and redistributing material out to distances of several AU (Salmeron and Ireland, 2012). Alternatively, CAIs may have formed near (<1 AU) the protoSun and been subsequently transported outward (>10 AU) due to the viscous evolution of the disk and turbulence effects within it (Cuzzi et al., 2003; Ciesla, 2007). After transport processes such as these brought CAIs into the outer solar system, they could have encountered relatively ^{17,18}O-rich environments such as may have been created, for example, by concentration of relatively ^{17,18}O-rich water near the snow line (Young, 2007).

The various CAI transport mechanisms discussed here are associated with astrophysical processes having characteristic timescales and heating times that are quite different from one another. Accordingly, O-isotopic profiles established by exchange during these different events should record different diffusion times. For example, the rapid FU outbursts occur very early, within <10 years of the beginning of the solar system (Boss et al., 2012) and heating times in disk winds are relatively short, ⩽30 years (Shu et al., 2001). Outward transport of CAIs from the inner to the outer nebular disk by diffusive processes takes much longer, 10^3–10^4 years (Cuzzi et al., 2003), and appears better matched to the timescales required to reproduce the O-isotopic profiles observed in Type A CAI interiors. The absolute time period may have been longer than the time required for diffusive exchange since diffusion calculations in this study only represent the integrated time at elevated temperatures and not necessarily the total time over which CAIs migrated within the protoplanetary disk (Fig. 9, Table 4). Likewise, the diffusive exchange could reflect hundreds or thousands of short heating events and/or maybe related to WL rim formation (e.g., Young et al., 2005), expected for particle transport by disk winds or within the shock fronts of density waves within the disk. It is also possible that radial excursions of CAIs across the inner edge of the disk gas produced both the mineralogical layering and O-isotopic variation of WL rims, due to the confluence of relatively ^{16}O-poor disk and ^{16}O-rich gas reservoirs (Park et al., 2012) and non-solar gas reservoirs that developed because of infall of outer disk material onto the protoSun through radial evaporation fronts (e.g., the snow line). Further work coordinating O-isotope profiles with

high precision Al–Mg chronology and measurements of more refractory stable isotopes (e.g., Mg and perhaps Ca) and Rare Earth Element abundance patterns, could help distinguish the roles of condensation, diffusive growth, and accumulation of preexisting dust grains as they relate to the astrophysical environments of WL rim formation and the alteration of CAI interiors in the nebula.

4.7. A general history of and summary of features of coarse-grained CAIs based on their oxygen isotope compositions

The studied inclusions imply the following formation history:

(1) Spinel data from A37 attest to the fact that some, and possibly all, CAIs initially formed from the protosolar oxygen isotopic composition ($\Delta^{17}O \sim -28‰$, McKeegan et al., 2011).
(2) The uniform intermediate composition ($\Delta^{17}O \sim -17$–$23‰$) of the interior melilite of A37 and spinel and fassaite in the interior of Type B CAI TS4 implies that some CAIs were exposed to a nebular gas of intermediate oxygen isotopic composition for up to 2×10^4 years, assuming oxygen exchange occurred at temperatures of 1400 K. This might reflect the reservoir that is typically considered "normal" for CAIs.
(3) The relatively ^{16}O-poor melilite interiors of all studied Type A CAIs indicate many CAIs were exposed to an ^{16}O-poor reservoir for as long as 5×10^3 to 3×10^4 -years, assuming temperatures of 1400 K. In total, a period of nearly 3.6×10^4 years is needed for the two exchange steps indicated by the oxygen record of A37, assuming temperatures of 1400 K. Two steps of exchange are also indicated by the Type B CAI TS4 data and could require a similar timescale, but it would be significantly shorter if equilibration with the intermediate reservoir in the first step occurred while the inclusion was still partially molten.
(4) The ^{16}O-poor interior of Type B CAI Egg-6 either reflects protracted exchange on the chondrite parent body or exchange with a planetary-like nebular gas in the solid-state, similar to that inferred for the Type A CAIs. If exchange occurred in the nebula, it would have required $\sim 3 \times 10^5$ years at 1400 K. Alternatively, if the isotopic compositions of the melilite in the interiors of the studied Type B CAIs reflect parent body processes, then much longer timescales ($>10^6$ years) are required even considering hydrothermal oxygen diffusion rates. The source of the required protracted heating remains elusive in either case, cf. Rubin (1995).
(5) The strong gradients in A37 and L6 toward planetary-like and relatively ^{16}O-rich compositions, respectively, likely occurred in a second step of nebular solid-state exchange (in #3). The protosolar environments documented by observations #1–5 may all predate rim formation, similar to the inclusions described in Yoshitake et al. (2005) and Aleon et al. (2007). A37 appears to record modification of the outermost melilite edge by a heating event (e.g., Wark and Boynton, 2001) that involved a relatively ^{16}O-poor, planetary-like reservoir, described as the earliest rim-forming event by Simon et al. (2011).
(6) Preservation of the strong gradients in A37 and L6 suggest circumstances where diffusive isotopic equilibration was limited and may indicate that these inclusions were rimmed relatively early and/or that they were rapidly accreted onto a parent body reducing the formation of dislocations from subsequent ionizing radiation.
(7) The relatively ^{16}O-enriched melilite margins of all studied Type A CAIs (except A37) indicate exposure to a relatively ^{16}O-rich nebular gas. It is possible that the strong gradients in A37 and L6, and the more subtle ones in Ef-1 and ALH3, actually reflect the effect of rim-forming processes.
(8) The spinel ± hibonite layer surrounding all studied CAIs reflects formation from a relatively ^{16}O-rich gas. Some spinel at the base of WL-rims may predate rim formation (Wark and Lovering, 1982). It remains unclear whether the spinel ± hibonite layer involves partial melting of the interior (Wark and Boynton, 2001) or whether it originates from the gas phase alone.
(9) Pyroxene layers outside the spinel ± hibonite layer can be heterogeneous in $\Delta^{17}O$, from relatively ^{16}O-rich to planetary-like, and they often record outward ("reverse") zoning toward more ^{16}O-rich compositions. This heterogeneity and sense of zoning is inconsistent with metasomatic growth in the nebula or on a parent body. It is likely that typical portions of WL rims condensed from several gas reservoirs with isotopically distinct compositions.
(10) The heterogeneous O-isotopic compositions in the olivine rim layers and in accretionary rims suggest that both types of olivine grew from relatively ^{16}O-rich and ^{16}O-poor gases (Krot et al., 2002).
(11) Finally, replacement of primary minerals by secondary minerals may have occurred in the nebula, e.g., Hutcheon and Newton (1981), and certainly occurred on the parent body. Distinguishing between these two end-member environments for given occurrences requires coordinated petrologic and isotopic studies.

5. CONCLUSIONS

The evolution of coarse-grained CAIs included open-system diffusive exchange with multiple, relatively ^{16}O-poor and ^{16}O-rich nebular gases, followed by Wark–Lovering rim formation, also from relatively ^{16}O-poor and ^{16}O-rich nebular gases, through condensation and possibly by the accumulation of preexisting nebular solids. The "normal" and "reverse" isotopic zoning profiles observed across the margins of refractory inclusions require that many CAIs contained in CV3 chondrites experienced at least a two-step nebular exchange history. Larger shifts toward

planetary-like O-isotope compositions in the melilite contained in Ef-1 and L6, both from reduced and more pristine chondrites, than in A37, an oxidized CV3 chondrite, indicate that oxygen exchange is decoupled from the formation of secondary alteration products. The $\Delta^{17}O$ record observed in WL rims is complicated, often exhibiting evidence of "reverse" O-isotopic zoning, and shifting from rather homogenous to extremely heterogeneous over short distances within and among mineral layering. Considered together with their changing mineral chemistry and textures, their $\Delta^{17}O$ values suggest that the rims grew under disequilibrium conditions in a dynamic, rather hot nebular environment. The complex WL rim on L6, composed of five distinct pyroxene layers and probably three distinct melilite zones with varying O-isotopic composition, demonstrates that some of the mineral layers formed sequentially, in discrete growth events. All of these observations support numerical disk models in which CAIs were transported between distinct nebular reservoirs multiple times over $\sim 10^3$–10^5 years prior to accretion onto a parent body. The relatively common occurrence of CAI phases with $\Delta^{17}O \approx -20‰$ may indicate the existence of an early and persistent, intermediate reservoir in which some inclusions re-equilibrated before, and in some cases after, initial WL rim growth.

ACKNOWLEDGMENTS

This work is dedicated to Dr. Ian Douglass Hutcheon (1947-2015), an exceptional scientist, mentor, and friend. He made significant contributions to this work, masterfully integrating intuition, open-mindedness, and skepticism. The remaining authors and many others in our community will sorely miss him. We are grateful to Journal Editor D. Papanastassiou and three anonymous reviewers for their careful and constructive reviews of this paper. The work was supported by NASA Cosmochemistry and Origins Programs: Grants NNH11ZDA66N to JIS, NNH10AO48I and NNH10AO05I to IDH, and NNX13AE73G to LG. Repolishing of several 'well-used' samples by Roger Harrington is gratefully appreciated. This work was performed under the auspices of the U.S. Department of Energy at Lawrence Livermore National Laboratory under Contract DE-AC52-07NA27344.

APPENDIX A. SUPPLEMENTARY DATA

Supplementary data associated with this article can be found, in the online version, at http://dx.doi.org/10.1016/j.gca.2016.04.025.

REFERENCES

Aleon J., El Goresy A. and Zinner E. (2007) Oxygen isotope heterogeneities in the earliest protosolar gas recorded in a meteoritic calcium–aluminum-rich inclusion. *Earth Planet. Sci. Lett.* **263**, 114–127.

Amelin Y., Krot A. N., Hutcheon I. D. and Ulyanov A. A. (2002) Lead isotopic ages of chondrules and calcium–aluminum-rich inclusions. *Science* **297**, 1678–1683.

Barber D. J., Martin P. M. and Hutcheon I. D. (1984) The microstructure of minerals in coarse-grained Ca–Al-rich inclusions from the Allende meteorite. *Geochim. Cosmochim. Acta* **48**, 769–783.

Bodénan J.-D., Starkey N. A., Russell S. S., Wright I. P. and Franchi I. A. (2014) An oxygen isotope study of Wark–Lovering rims on type A CAIs in primitive carbonaceous chondrites. *Earth Planet. Sci. Lett.* **401**, 327–336.

Bonal L., Quirico E., Bourot-Denise M. and Montagnac G. (2006) Determination of the petrologic type of CV3 chondrites by Raman spectroscopy of included organic matter. *Geochim. Cosmochim. Acta* **70**, 1849–1863.

Boss A. P., Alexander C. M. O. D. and Podolak M. (2012) Cosmochemical consequences of particle trajectories during FU Orionis outburst by the early Sun. *Earth Planet. Sci. Lett.* **345–348**, 18–26.

Boss A. P. (2004) Evolution of the solar nebula. VI. Mixing and transport of isotopic heterogeneity. *Astrophys. J.* **616**, 1265–1277.

Bouvier A. and Wadhwa M. (2010) The age of the Solar System redefined by the oldest Pb–Pb age of a meteoritic inclusion. *Nat. Geosci.* **3**, 637–641.

Boynton W. V. and Wark D. A. (1985) Refractory rims: evidence for high temperature events in the post-formation history of Ca, Al-rich inclusions. *Meteoritics* **20**, 613–614.

Brearley A. J. and Jones R. H. (1998) Chondritic meteorites. In *Planetary Materials* (ed. J. J. Papike). Mineralogical Society of America, Washington, D.C., pp. 1–398.

Brearley A. (1997) Disordered biopyriboles, amphibole, and talc in the allende meteorite: products of nebular or parent body aqueous alteration. *Science* **276**, 1103–1105.

Brownlee D., Tsou P., Aleon J., Alexander C. M. O., Araki T., Bajt S., Baratta G. A., Bastien R., Bland P., Bleuet P., Borg J., Bradley J. P., Brearley A., Brenker F., Brennan S., Bridges J. C., Browning N. D., Brucato J. R., Bullock E., Burchell M. J., Busemann H., Butterworth A., Chaussidon M., Cheuvront A., Chi M. F., Cintala M. J., Clark B. C., Clemett S. J., Cody G., Colangeli L., Cooper G., Cordier P., Daghlian C., Dai Z. R., D'Hendecourt L., Djouadi Z., Dominguez G., Duxbury T., Dworkin J. P., Ebel D. S., Economou T. E., Fakra S., Fairey S. A. J., Fallon S., Ferrini G., Ferroir T., Fleckenstein H., Floss C., Flynn G., Franchi I. A., Fries M., Gainsforth Z., Gallien J. P., Genge M., Gilles M. K., Gillet P., Gilmour J., Glavin D. P., Gounelle M., Grady M. M., Graham G. A., Grant P. G., Green S. F., Grossemy F., Grossman L., Grossman J. N., Guan Y., Hagiya K., Harvey R., Heck P., Herzog G. F., Hoppe P., Horz F., Huth J., Hutcheon I. D., Ignatyev K., Ishii H., Ito M., Jacob D., Jacobsen C., Jacobsen S., Jones S., Joswiak D., Jurewicz A., Kearsley A. T., Keller L. P., Khodja H., Kilcoyne A. L. D., Kissel J., Krot A., Langenhorst F., Lanzirotti A., Le L., Leshin L. A., Leitner J., Lemelle L., Leroux H., Liu M. C., Luening K., Lyon I., MacPherson G., Marcus M. A., Marhas K., Marty B., Matrajt G., McKeegan K., Meibom A., Mennella V., Messenger K., Messenger S., Mikouchi T., Mostefaoui S., Nakamura T., Nakano T., Newville M., Nittler L. R., Ohnishi I., Ohsumi K., Okudaira K., Papanastassiou D. A., Palma R., Palumbo M. E., Pepin R. O., Perkins D., Perronnet M., Pianetta P., Rao W., Rietmeijer F. J. M., Robert F., Rost D., Rotundi A., Ryan R., Sandford S. A., Schwandt C. S., See T. H., Schlutter D., Sheffield-Parker J., Simionovici A., Simon S., Sitnitsky I., Snead C. J., Spencer M. K., Stadermann F. J., Steele A., Stephan T., Stroud R., Susini J., Sutton S. R., Suzuki Y., Taheri M., Taylor S., Teslich N., Tomeoka K., Tomioka N., Toppani A., Trigo-Rodriguez J. M., Troadec D., Tsuchiyama A., Tuzzolino A. J., Tyliszczak T., Uesugi K., Velbel M., Vellenga J., Vicenzi E., Vincze L., Warren J., Weber I., Weisberg M., Westphal A. J., Wirick S., Wooden D., Wopenka B., Wozniakiewicz P., Wright I., Yabuta H., Yano H., Young

E. D., Zare R. N., Zega T., Ziegler K., Zimmerman L., Zinner E. and Zolensky M. (2006) Research article – Comet 81P/Wild 2 under a microscope. *Science* **314**, 1711–1716.

Bullock E. S., MacPherson G. J., Nagashima K., Krot A. N., Petaev M. I., Jacobsen S. B. and Ulyanov A. A. (2012) Forsterite-bearing type B refractory inclusions from CV3 chondrites: aggregates to volatilized melt droplets. *Meteorit. Planet. Sci.* **47**, 2128–2147.

Bullock E. S., Knight K. B., Richter F. M., Kita N. T., Ushikubo T., MacPherson G. J., Davis A. M. and Mendybaev R. A. (2013) Mg and Si isotopic fractionation patterns in types B1 and B2 CAIs: implications for formation under different nebular conditions. *Meteorit. Planet. Sci.* **48**, 1440–1458.

Chaussidon M., Libourel G. and Krot A. N. (2008) Oxygen isotopic constraints on the origin of magnesian chondrules and on the gaseous reservoirs in the early Solar System. *Geochim. Cosmochim. Acta* **72**, 1924–1938.

Ciesla F. J. (2007) Outward transport of high-temperature materials around the midplane of the solar nebula. *Science* **318**, 613–615.

Clarke, Jr., R. S., Jarosewich E., Mason B., Nelen J., Gomez M. and Hyde J. R. (1970) The Allende, Mexico meteorite shower. *Smithsonian Contrib. Earth Sci.* **5**(1970), 1–53.

Clayton R. N., Onuma N., Grossman L. and Mayeda T. K. (1977) Distribution of the pre-solar component in Allende and other carbonaceous chondrites. *Earth Planet. Sci. Lett.* **34**, 209–224.

Clayton R. N. (2002) Solar System – self-shielding in the solar nebula. *Nature* **415**, 860–861.

Connelly J. N., Bizzarro M., Krot A. N., Nordlund A., Wielandt D. and Ivanova M. A. (2012) The absolute chronology and thermal processing of solids in the solar protoplanetary disk. *Science* **338**, 651–655.

Cosarinsky M., Taylor D. J., McKeegan K. D. and Hutcheon I. D. (2005) Mg isotopic study of Wark–Lovering rims in Type A inclusions from CV chondrites: formation mechanisms and timing. *68th Annual Meteoritical Society Meeting*. p. Abst. #5284.

Cosarinsky M., Leshin L. A., MacPherson G. J., Guan Y. and Krot A. N. (2008) Chemical and oxygen isotopic compositions of accretionary rim and matrix olivine in CV chondrites: constraints on the evolution of nebular dust. *Geochim. Cosmochim. Acta* **72**, 1887–1913.

Crank J. (1975) *The Mathematics of Diffusion*, 2nd ed. Clarendon Press, Oxford, p. 91, eqn. 6.

Cuzzi J. N., Davis S. S. and Dobrovolskis A. R. (2003) Blowing in the wind. II. Creation and redistribution of refractory inclusions in a turbulent protoplanetary nebula. *Icarus* **166**, 385–402.

Dominguez G. (2010) A heterogeneous chemical origin for the ^{16}O-enriched and ^{16}O-depleted reservoirs of the early solar system. *Astrophys. J. Lett.* **713**, L59–L63.

Dyl K. A., Simon J. I. and Young E. D. (2011) Valence state of titanium in the Wark–Lovering rim of a Leoville CAI as a record of progressive oxidation in the early Solar Nebula. *Geochim. Cosmochim. Acta* **75**, 937–949.

Fagan T. J., Krot A., Keil K. and Yurimoto H. (2004a) Oxygen isotope alteration in Ca-Al-rich inclusions from Efremovka: nebular or parent body setting? *Meteorit. Planet. Sci.* **39**, 1257–1272.

Fagan T. J., Krot A. N., Keil K. and Yurimoto H. (2004b) Oxygen isotopic evolution of amoeboid olivine aggregates in the reduced CV3 chondrites Efremovka, Vigarano, and Leoville. *Geochim. Cosmochim. Acta* **68**, 2591–2611.

Fahey A. J., Goswami J. N., McKeegan K. D. and Zinner E. (1987a) Al-26, Pu-244, Ti-50, REE, and trace-element abundances in hibonite grains from CM and CV meteorites. *Geochim. Cosmochim. Acta* **51**, 329–350.

Fahey A. J., Zinner E. Z., Crozaz G. and Kornacki A. S. (1987b) Microdistributions of Mg isotopes and REE abundances in a Type A calcium–aluminum-rich inclusion from Efremovka. *Geochim. Cosmochim. Acta* **51**, 3215–3229.

Fedkin A. V. and Grossman L. (2006) The fayalite content of chondritic olivine: obstacle to understanding the condensation of rocky material. In *Meteorites and the Early Solar System II* (eds. D. Lauretta and H. Y. J. McSween). University of Arizona Press, Tucson, AZ, pp. 279–294.

Grossman L., Ebel D. S. and Simon S. B. (2002) Formation of refractory inclusions by evaporation of condensate precursors. *Geochim. Cosmochim. Acta* **66**, 145–161.

Grossman L., Simon S. B., Rai V. K., Thiemens M. H., Hutcheon I. D., Williams R. W., Galy A., Ding T., Fedkin A. V., Clayton R. N. and Mayeda T. K. (2008) Primordial compositions of refractory inclusions. *Geochim. Cosmochim. Acta* **72**, 3001–3021.

Grossman L. (1972) Condensation in the primitive solar nebula. *Geochim. Cosmochim. Acta* **36**, 597–619.

Han J. and Brearley A. J. (2012) The microstructure and microchemistry of amoeboid olivine aggregates from the ALHA 77307 CO3.0 carbonaceous chondrite: constraints on formation and thermal histories. *43rd Lunar and Planetary Science Conference*. Abstr. #1323.

Hsu W. B., Wasserburg G. J. and Huss G. R. (2000) High time resolution by use of the Al-26 chronometer in the multistage formation of a CAI. *Earth Planet. Sci. Lett.* **182**, 15–29.

Huss G. R., Meshik A. P., Smith J. B. and Hohenberg C. M. (2003) Presolar diamond, silicon carbide, and graphite in carbonaceous chondrites: implications for thermal processing in the solar nebula. *Geochim. Cosmochim. Acta* **67**, 4823–4848.

Huss G. R., Rubin A. E. and Grossman J. N. (2006) Thermal metamorphism in chondrites. In *Meteorites and the Early Solar System II* (eds. D. S. Lauretta and H. Y. McSween). University of Arizona Press, pp. 567–586.

Hutcheon I. D. and Newton R. C. (1981) Mg isotopes, mineralogy, and mode of formation of secondary phases in C3 refractory inclusions. *12th Lunar and planetary Science Conference*. pp. 491–493.

Hutcheon I. D., Krot A. N., Keil K., Phinney D. L. and Scott E. R. D. (1998) ^{53}Mn–^{53}Cr dating of fayalite formation in the CV3 chondrite Mokoia: evidence for asteroidal alteration. *Science* **282**, 1865–1867.

Ingrin J., Pacaud L. and Jaoul O. (2001) Anisotropy of oxygen diffusion in diopside. *Earth Planet. Sci. Lett.* **192**, 347–361.

Ito M., Messenger S., Keller L. P., Rahman Z. U., Ross D. K. and Nakamura-Messenger K. (2010) FIB-NanoSIMS-TEM coordinated study of a Wark–Lovering rim in a Vigarano Type A CAI. *41st Lunar and Planetary Science Conference*. Abst. 1177.

Keil K., Stoffler D., Love S. G. and Scott E. R. D. (1997) Constrains on the role of impact heating and melting in asteroids. *Meteorit. Planet. Sci.* **32**, 349–363.

Keller L. P. and Buseck P. R. (1991) Calcic micas in the Allende meteorite: evidence for hydration reactions in the early Solar nebula. *Science* **252**, 947–949.

Keller L. P., Needham A.W. and Messenger S. (2013) A FIB/TEM study of a complex Wark–Lovering rim on a Vigarano CAI, Meteoritical Society. Abst #5300, Edmonton.

Krot A. N., McKeegan K. D., Leshin L. A., MacPherson G. J. and Scott E. R. D. (2002) Existence of an ^{16}O-Rich Gaseous Reservoir in the Solar Nebula. *Science* **295**, 1051–1054.

Krot A. N., Nagashima K., Ciesla F. J., Meyer B. S., Hutcheon I. D., Davis A. M., Huss G. R. and Scott E. R. D. (2010) Oxygen isotopic composition of the Sun and mean oxygen isotopic composition of protosolar silicate dust: evidence from refractory inclusions. *Astrophys. J.* **713**, 1159–1166.

Kunihiro T., Rubin A. E., McKeegan K. D. and Wasson J. T. (2004) Initial $^{26}Al/^{27}Al$ in carbonaceous-chondrite chondrules: too little ^{26}Al to melt asteroids. *Geochim. Cosmochim. Acta* **68**, 2947–2957.

Kwok S., Purton C. R. and FitzGerald P. M. (1978) On the origin of planetary nebulae*. *Astrophys. J.* **219**, L125–L127.

LaTourrette T. and Hutcheon I. D. (1999) Mg diffusion in melilite: thermal histories for CAIs and their parent bodies. *Lunar and Planetary Science Conference XXX*. Abst #2003.

Liang Y., Richter F. M., Davis A. M. and Watson E. B. (1996) Diffusion in silicate melts 1. Self diffusion in $CaO–Al_2O_3–SiO_2$ at 1500 °C and 1 GPa. *Geochim. Cosmochim. Acta* **60**, 4353–4367.

Lyons J. R. and Young E. D. (2005) CO self-shielding as the origin of oxygen isotope anomalies in the early solar nebula. *Nature* **435**, 317–320.

MacPherson G. J. and Davis A. M. (1993) A petrologic and ion microprobe study of a vigarano Type-B refractory inclusion – evolution by multiple stages of alteration and melting. *Geochim. Cosmochim. Acta* **57**, 231–243.

MacPherson G. J., Grossman L., Allen J. M. and Beckett J. R. (1981). Origin of rims on coarse-grained inclusions in the Allende meteorite. *Proceedings of Lunar Science Conference 12th*. pp. 1079–1091.

MacPherson G. J., Hashimoto A. and Grossman L. (1985) Accretionary rims on inclusions in the Allende meteorite. *Geochim. Cosmochim. Acta* **49**, 2267–2279.

MacPherson G. J., Kita N. T., Ushikubo T., Bullock E. S. and Davis A. M. (2012) Well-resolved variations in the formation ages for Ca–Al-rich inclusions in the early Solar System. *Earth Planet. Sci. Lett.* **331–332**, 43–45.

Mahon K. I. (1996) The New "York" regression: application of an improved statistical method to geochemistry. *Int. Geol. Rev.* **38**, 293–303.

Matzel J. E. P., Simon J. I., Hutcheon I. D., Jacobsen B., Simon S. B. and Grossman L. (2013) Oxygen isotope measurements of a rare Murchison Type A CAI and its rim. *44th Lunar and Planetary Science Conference*. p. Abst. #2632.

McKeegan K. D., Aleon J., Bradley J., Brownlee D. and Team Stardust. (2006) Isotopic compositions of cometary matter returned by stardust. *Science* **314**, 1724–1728.

McKeegan K. D., Kallio A. P. A., Heber V. S., Jarzebinski G., Mao P. H., Coath C. D., Kunihiro T., Wien R. C., Nordhort J. E., Moses, Jr., R. W., Reisenfeld D. B., Jurewicz A. J. G. and Burnett D. S. (2011) The oxygen Isotopic composition of the Sun inferred from captured solar wind. *Science* **332**, 1528–1532.

Meeker G. P., Wasserburg G. J. and Armstrong J. T. (1983) Replacement textures in CAI and implications regarding planetary metamorphism. *Geochim. Cosmochim. Acta* **47**, 707–721.

Metzler K., Bischoff A. and Stöffler D. (1992) Accretionary dust mantles in CM chondrites: evidence for solar nebula processes. *Geochim. Cosmochim. Acta* **56**, 2873–2897.

Park C., Wakaki S., Sakamoto N., Kobayashi S. and Yurimoto H. (2012) Oxygen isotopic composition of the solar nebula gas inferred from high-precision isotope imagine of melilite crystals in an Allende CAI. *Meteorit. Planet. Sci.* **47**, 2070–2083.

Pouchou J. L. and Pichoir F. (1984) A new model for quantitative X-ray microanalysis. Part I: application to the analysis of homogeneous samples. *Rech. Aerosp.* **3**, 13–38.

Rubin A. E. (1995) Petrologic evidence for collisional heating of chondritic asteroids. *Icarus* **113**, 156–167.

Ruzicka A. (1997) Mineral layers around coarse-grained, Ca–Al-rich inclusions in CV3 carbonaceous chondrites: formation by high-temperature metasomatism. *J. Geophys. Res.* **102**, 13, 387–313, 402.

Ryerson F. J. and McKeegan K. D. (1994) Determination of oxygen self-diffusion in akermanite, anorthite, diopside, and spinel – implications for oxygen isotopic anomalies and the thermal histories of Ca–Al-rich inclusions. *Geochim. Cosmochim. Acta* **58**, 3713–3734.

Sakamoto N., Seto Y., Itoh S., Kuramoto K., Fujino K., Nagashima K., Krot A. N. and Yurimoto H. (2007) Remnants of the early solar system water enriched in heavy oxygen isotopes. *Science* **317**, 231–233.

Salmeron R. and Ireland T. (2012) The role of protostellar jets in star formation and the evolution of the early solar system: astrophysical and meteoritical perspectives. *Meteorit. Planet. Sci.* **47**, 1922–1940.

Shu F. H., Shang H. and Lee T. (1996) Toward an astrophysical theory of chondrites. *Science* **271**, 1545–1552.

Shu F. H., Shang H., Gounelle M., Glassgold A. E. and Lee T. (2001) The origin of chondrules and refractory inclusions in chondritic meteorites. *Astrophys. J.* **548**, 1029–1050.

Simon J. I. and DePaolo D. J. (2010) Stable calcium isotopic composition of meteorites and rocky planets. *Earth Planet. Sci. Lett.* **289**, 457–466.

Simon S. B. and Grossman L. (2013) A compact type A inclusion with multiple Wark–Lovering rims: a complex history recorded in pyroxene. *44th Lunar and Planetary Science Conference*. Lunar and Planetary Institute, Houston, p. Abs #2793.

Simon J. I. and Young E. D. (2011) Resetting, errorchrons and the meaning of canonical CAI initial $^{26}Al/^{27}Al$ values. *Earth Planet. Sci. Lett.* **304**, 468–482.

Simon S. B., Davis A. M. and Grossman L. (1999) Origin of compact type A refractory inclusions from CV3 carbonaceous chondrites. *Geochim. Cosmochim. Acta* **63**, 1233–1248.

Simon S. B., Davis A. M. and Grossman L. (2001) Formation of orange hibonite, as inferred from some Allende inclusions. *Meteorit. Planet. Sci.* **36**, 331–350.

Simon S. B., Grossman L. and Davis A. M. (1991) Fassaite composition trends during crystallization of Allende Type B inclusion melts. *Geochim. Cosmochim. Acta* **55**, 2635–2655.

Simon J. I., Young E. D., Russell S. S., Tonui E. K., Dyl K. A. and Manning C. E. (2005) A short timescale for changing oxygen fugacity in the solar nebula revealed by high-resolution Al-26–Mg-26 dating of CAI rims. *Earth Planet. Sci. Lett.* **238**, 272–283.

Simon J. I., Hutcheon I. D., Simon S. B., Matzel J. E. P., Ramon E. C., Weber P. K., Grossman L. and DePaolo D. J. (2011) Oxygen isotope variations at the margin of a CAI records circulation within the solar nebula. *Science* **331**, 1175–1178.

Stolper E. (1982) Crystallization sequences of Ca–Al-rich inclusions from Allende: an experimental study. *Geochim. Cosmochim. Acta* **46**, 2159–2180.

Wark D. A. and Boynton W. V. (2001) The formation of rims on calcium–aluminum-rich inclusions: step I-flash heating. *Meteorit. Planet. Sci.* **36**, 1135–1166.

Wark D. A. and Lovering J. F. (1977) Marker events in the early evolution of the solar system: evidence from rims on Ca–Al-rich inclusions in carbonaceous chondrites. *Proceedings of Lunar Science Conference 8th*. pp. 95–112.

Wark D. A. and Lovering J. F. (1982) Evolution of Ca-, Al-rich bodies in the earliest solar system: growth by incorporation. *Geochim. Cosmochim. Acta* **46**, 2595–2607.

Wasserburg G. J., Typhoon L. and Papanastassiou D. A. (1977) Correlated O and Mg isotopic anomalies in Allende inclusions: II. Magnesium. *Geophys. Res. Lett.* **4**, 299–302.

Wasson J. T., Yurimoto H. and Russell S. S. (2001) ^{16}O-rich melilite in CO3.0 chondrites: possible formation of common,

^{16}O-poor melilite by aqueous alteration. *Geochim. Cosmochim. Acta* **65**, 4539–4549.

Yoshitake M., Koide Y. and Yurimoto H. (2005) Correlations between oxygen-isotopic composition and petrologic setting in a coarse-grained Ca, Al-rich inclusion. *Geochim. Cosmochim. Acta* **69**, 2663–2674.

Young E. D., Simon J. I., Galy A., Russell S. S., Tonui E. and Lovera O. (2005) Supra-canonical Al-26/Al-27 and the residence time of CAIs in the solar protoplanetary disk. *Science* **308**, 223–227.

Young E. D. (2001) The hydrology of carbonaceous chondrite parent bodies and the evolution of planet progenitors. *Royal Soc.* **359**, 2095–2110.

Young E. D. (2007) Time-dependent oxygen isotopic effects of CO self shielding across the solar protoplanetary disk. *Earth Planet. Sci. Lett.* **2007**, 468–483.

Yurimoto H. and Kuramoto K. (2004) Molecular cloud origin for the oxygen isotope heterogeneity in the solar system. *Science* **305**, 1763–1766.

Yurimoto H., Morioka M. and Nagasawa H. (1989) Diffusion in single crystals of melilite: I. Oxygen. *Geochim. Cosmochim. Acta* **53**, 2387–2394.

Yurimoto H., Ito M. and Nagahara H. (1998) Oxygen isotope exchange between refractory inclusion in Allende and Solar Nebula Gas. *Science* **282**, 1874–1876.

Associate editor: Dimitri A. Papanastassiou